

Facultad de Ciencias

Study of the tunneling effect in ferroelastic transitions in systems with cooperative Jahn-Teller effect

(Estudio del efecto túnel en transiciones ferroelásticas en sistemas con Jahn-Teller cooperativo)

Trabajo de Fin de Grado para acceder al

GRADO EN FÍSICA

Autor: Pablo Miguel Rubio

Director: Pablo García Fernández

Julio - 2025

Agradecimientos

En primer lugar, quiero agradecer a todos mis profesores a lo largo de la carrera. Sin ellos, además de que este trabajo no habría sido posible, no habría podido disfrutar de la Física como lo he hecho. En especial, quiero agradecer a Pablo García Fernández, mi director, por su infinita paciencia y por haber dedicado tantísimo tiempo a ayudarme en la realización de este trabajo. El trabajo no habría sido posible sin su ayuda y apoyo constante.

También quiero agradecer a mis compañeros de clase, sobre todo a aquellos con los que he jugado tantísimas partidas al mus y que tras estos años en la carrera me han acompañado y acogido como uno más. Quiero agradecer personalmente a Mikel, Pablo, Pepe y Emilio, por haberme dado el gusto de poder compartir piso con vosotros, por todas las cenas y películas, por las risas y los momentos compartidos. Y, por supuesto, también quiero dar las gracias a Julen, quien se ha pasado tantos días de verano conmigo en la biblioteca durante la realización de este trabajo.

Por último, quiero agradecer a mi familia. A mis padres, por haberme dado la oportunidad de estudiar lo que me gusta y por haberme apoyado en todo momento. A Asier, mi hermano, por haber estado siempre ahí. Y a mis amamas y a izeko, por haberme apoyado en todo momento. Os quiero mucho.

Abstract

The quantum tunneling effect is the phenomenon where a particle can pass through a potential barrier that it classically should not be able to cross. This effect is crucial in understanding various physical processes, like the umbrella inversion in ammonia and the energy splitting involved with it. On the other hand, the Jahn-Teller effect is the spontaneous distortion of a molecule or crystal due to the degeneracy of its electronic states. This distortion can lower the symmetry and lift the degeneracy of the system. The main goal of this work is to analyze the tunneling dynamics in both JT and non-JT systems and compute the tunneling period that would allow us to observe the tunneling, a microscopic feature, through a macroscopic measurement, such as the crystal's form. In order to achieve this a computational solution based on a finite difference method has been developed and it has been applied to study the tunneling dynamics in KCuF₃, a prototypical material that exhibits the cooperative Jahn-Teller effect. In addition to this, the tunneling dynamics of other systems such as impurities in oxides and triatomic molecules have also been explored.

Keywords: Quantum Tunneling, Jahn-Teller Effect, Ferroelasticity, KCuF₃, Perovskite, Finite Difference Method.

Resumen

El túnel cuántico es el fenómeno por el cual una partícula puede atravesar una barrera de potencial que, clásicamente, no debería ser capaz de superar. Este efecto es crucial para comprender diversos procesos físicos, como la inversión de la forma de paraguas del amoniaco y el desdoblamiento de energías asociado a ella. Por otro lado, el efecto Jahn-Teller consiste en la distorsión espontánea de una molécula o un cristal debido a la degeneración de sus estados electrónicos. Esta distorsión puede reducir la simetría y romper la degeneración del sistema. El objetivo principal de este trabajo es analizar la dinámica de túnel tanto en sistemas con JT como en sistemas sin JT, y calcular el período del efecto túnel, un fenómeno microscópico, a través de una medida macroscópica, como la forma del cristal. Para ello se ha desarrollado una solución computacional basada en el método de diferencias finitas, que se ha aplicado al estudio de la dinámica de túnel en KCuF₃, un material prototípico que presenta el efecto Jahn-Teller cooperativo. Además de esto, también se han explorado las dinámicas de túnel en otros sistemas, como impurezas en óxidos y moléculas triatómicas.

Palabras clave: Tunelamiento Cuántico, Efecto Jahn-Teller, Ferroelasticidad, KCuF₃, Perovskita, Método de Diferencias Finitas.

Contents

1	Intr	roduction	1
	1.1	Quantum Tunneling Effect	1
	1.2	Why KCuF ₃ : Jahn-Teller Effect and Ferroelasticity	3
	1.3	Objectives	5
	1.4	Structure of this work	6
2	\mathbf{Vib}	pronic Coupling Theory	7
	2.1	The Hamiltonian	7
	2.2	Adiabatic approximation	8
		2.2.1 Jahn-Teller systems	9
		2.2.2 Warping and higher order terms	14
3	Cor	mputational Methods	16
	3.1	First Principles	16
		3.1.1 Hartree-Fock	16
		3.1.2 Density Functional Theory	18
	3.2	CRYSTAL	20
4	Res	sults	22
	4.1	Nuclear dynamics in JT systems	22
		4.1.1 Non-warped system solution	22
		4.1.2 Tunneling dynamics in JT systems	23
		4.1.3 Non-Jahn-Teller Systems	28
	4.2	Computational Solution of the $E \otimes e$ Jahn-Teller Problem	28
		4.2.1 Finite differences method	28
		4.2.2 Program output	31
		4.2.3 Polar coordinates	32
	4.3	Obtention of coupling constants and tunneling splitting	35
		4.3.1 KCuF ₃	35
		4.3.2 JT in impurities and molecules	40
5	Cor	nclusions	49
\mathbf{A}	\mathbf{JT}	System Python Code	50
R	Nor	n-JT System Python Code	53

Chapter 1

Introduction

1.1 Quantum Tunneling Effect

Quantum tunneling is one of the most fascinating phenomena in quantum mechanics. It refers to the ability of a particle to pass through a potential barrier, even if it does not have enough energy to overcome the barrier classically [1]. This happens due to the nature of quantum mechanics, where particles are defined with a wavefunction that measures their probability amplitude. Tunneling is the name of the phenomenon associated to particles having a non-zero probability of being found on the other side of the barrier. This effect is not a mathematical artifact, but a real observable property and it has been experimentally verified in many different systems.

A fundamental example is the tunneling in ammonia molecules (NH₃). Ammonia has a pyramidal structure with a nitrogen atom at the apex and three hydrogen atoms at the base (See Figure 1.1, Left). The nitrogen ion can be found on either side of the plane formed by the three hydrogen ions, and the two configurations are equivalent, both of energy E_0 . Let us denote by $|\uparrow\rangle$ the configuration where the nitrogen ion is above the plane and by $|\downarrow\rangle$ the configuration where it is below the plane. The shape of NH₃ is commonly known as the umbrella shape due to the resemblance with an umbrella. Classically, the nitrogen atom would need to overcome a potential barrier to move from one side of the plane to the other, i.e. to transition from $|\uparrow\rangle$ to $|\downarrow\rangle$, but quantum mechanically, it can just tunnel through the barrier. Due to tunneling effect both states can "communicate" and coexist in a superposition of the two configurations:

$$|\Psi\rangle = \alpha |\uparrow\rangle + \beta |\downarrow\rangle. \tag{1.1}$$

The tunneling leads to two eigenstates, the stationary states of the system, which are symmetric and antisymmetric combinations of the two configurations:

$$|+\rangle = \frac{1}{\sqrt{2}}(|\uparrow\rangle + |\downarrow\rangle),$$
 (1.2)

$$|-\rangle = \frac{1}{\sqrt{2}}(|\uparrow\rangle - |\downarrow\rangle). \tag{1.3}$$

And these two eigenstates slightly differ in energies, the symmetric state $|+\rangle$ being lower in energy than the antisymmetric state $|-\rangle$. In particular, the symmetric state $|+\rangle$ has an energy of $E_{-}=E_{0}-A$ and the antisymmetric state $|-\rangle$ has an energy of $E_{+}=E_{0}+A$, and the difference between the two of them is 2A (See Figure 1.1, Right). Therefore, quantum tunneling can produce a splitting of the energy levels, often called tunneling splitting (and originally called inversion splitting due to this phenomenon in ammonia as the motion of the nitrogen ion is known as the umbrella inversion of NH₃).

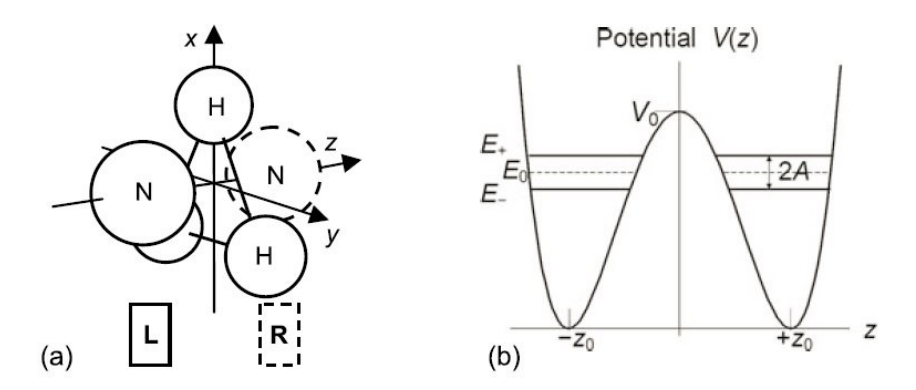


Figure 1.1: Left: Pyramidal structure of ammonia (NH₃), the continuous line indicates the position of the nitrogen atom in the $|\downarrow\rangle$ configuration while the dotted line indicates the equivalent position of the nitrogen atom in the $|\uparrow\rangle$ configuration. Right: Tunneling splitting in ammonia. The figure shows the potential energy surface V(z) that separates both configurations with the energy barrier in the middle. The energy of the equivalent states E_0 is indicated, as well as the split levels E_- and E_+ , and the energy difference 2A. Figure obtained from [2].

This tunneling splitting in ammonia has an associated energy difference of about 10^{-4} eV [2], which corresponds to a frequency of about 24 GHz. This frequency is in the range of microwave radiation, and it is the basis of the ammonia MASER (Microwave Amplification by Stimulated Emission of Radiation), a device that produces coherent microwave radiation. The ammonia MASER was one of the first MASERs ever built, and it was a precursor to the development of the LASER [3].

Throughout the undergraduate studies, the importance of the Born-Oppenheimer (or adiabatic) approximation has been much emphasized. This approximation allows for the separation of electronic and nuclear motions to describe every structure of matter, and the solids in particular. The basic idea is that since the nuclei are much heavier than the electrons, they move much more slowly, and thus electrons react almost instantaneously to atomic motions. However, many systems exhibit phenomena that are impossible to explain if this simplification is considered. In this work, we will explore situations where this separation is not valid.

The example of ammonia illustrates that quantum tunneling allows atoms to move around in ways that are not possible in classical mechanics. However, in many cases, these effects are influenced by the electronic structure of the system. In such systems, where atomic vibrations and electronic movement are mutually dependent, new phenomena can appear, such as the *Berry Phase*.

The Berry phase is the phase acquired by a wavefunction when the system undergoes a cyclic, slow (adiabatic) process [4]. When a system is subjected to a process in which the parameters are varied slowly and starts and ends in the same configuration, the wavefunction may acquire a geometric phase factor, which is not related to any dynamical evolution of the system and is closely related to the presence of conical intersections (As we will discuss in more detail in Chapter 2) in the adiabatic potential energy surface (APES) [4]. Therefore being called a geometrical or topological phase. The presence or absence of this Berry Phase can reverse the expected tunnel-split energy levels (See Figure 1.2) of a given system [5], and therefore it affects the tunneling dynamics.

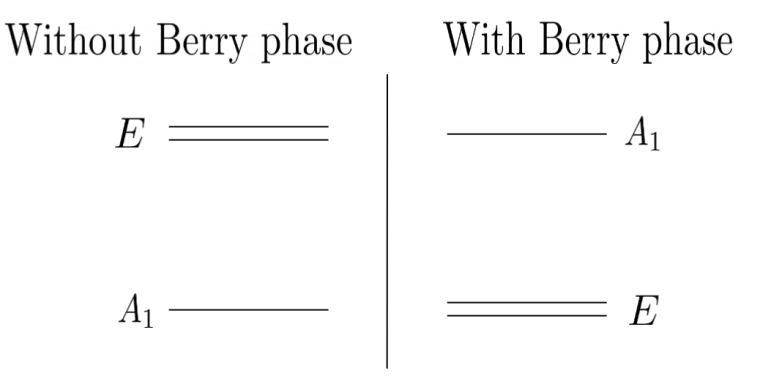


Figure 1.2: Illustration of the Berry Phase effect in a two-level system. Left: Without Berry Phase, the A_1 state is lower in energy than the E states. Right: With Berry Phase, the E states are lower in energy than the A_1 state.

So far, we have discussed the role of quantum tunneling and the Berry Phase in molecular systems, but in principle, it could be present in macroscopic systems, like solids. In solids, the cooperative dynamics of ions could show quantum processes. A paradigmatic example of a system where this is observed is the KCuF₃ perovskite. A crucial aspect is the tunneling's frequency: if the coupling between electrons and nuclei is strong enough, the system can oscillate between different configurations in an accessible time scale, and maybe being able to observe it in macroscopic magnitudes such as the lattice parameters. This spontaneous change of configurations can lead to phenomena like ferroelasticity and the ability to observe quantum phenomena like superposition in macroscopic objects.

1.2 Why KCuF₃: Jahn-Teller Effect and Ferroelasticity

The Jahn-Teller Effect (JTE) is a phenomenon that occurs in molecules and crystals with degenerate electronic states. In order to lift the degeneracy, the system undergoes a distortion of its geometry, generally to a lower symmetry one. For instance, if we consider a system with a cubic symmetry, the JTE can lead to a spontaneous tetragonal distortion, in the form of elongation (or compression) of one of the axes of the cube.

KCuF₃ is a canonical example of a material where the JTE is significant. It is a perovskite, that is, a material with the general formula ABX₃, where A and B are two different cations and X is an anion. In KCuF₃, the potassium (K) ion is usually in the center of the cubic structure of the perovskite, the copper (Cu) ions are located at the corners of the cube, and the fluorine (F) ions are set in the centers of the edges of the cube, forming an octahedron around the copper (See Figure 1.3).

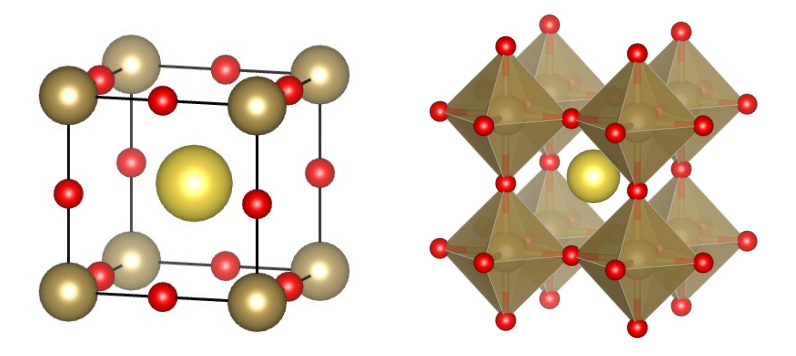


Figure 1.3: Left: Illustration of the KCuF₃ crystal structure. The Cu²⁺ ions are in brown surrounded by F⁻ ions in red, with K⁺ ions yellow. Right: Crystalline structure of KCuF₃. Images obtained with software VESTA (Courtesy of M. Solaguren).

In KCuF₃, the Cu²⁺ ions are in a d^9 electronic configuration, which leads to a doubly-degenerate e_g state. This is because the d orbitals are split into two sets of energy levels: the lower-energy, triply-degenerate t_{2g} orbitals and the higher-energy, doubly-degenerate e_g orbitals (See Figure 1.4, Left). Since each energy level can accommodate two electrons (with opposite spins), the first six electrons will occupy the t_{2g} orbitals, while the remaining three electrons will occupy the e_g orbitals, leaving one vacant state. We are left with four possibilities (See Figure 1.4, Right) for the last electron: a two-fold spatial degeneracy of the e_g orbitals, often denoted θ and ε , and a two-fold spin degeneracy, up and down. This is commonly denoted as 2E_g . For the first order vibronic terms (See Chapter 2) to be non-zero, the atomic vibrations must also transform as e-type vibrational modes [4]. Therefore the name $E \otimes e$ Jahn-Teller problem. In KCuF₃, the e-type vibrational modes correspond to distortions of the CuF⁴⁻₆ octahedra, which can be tetragonal or orthorhombic.

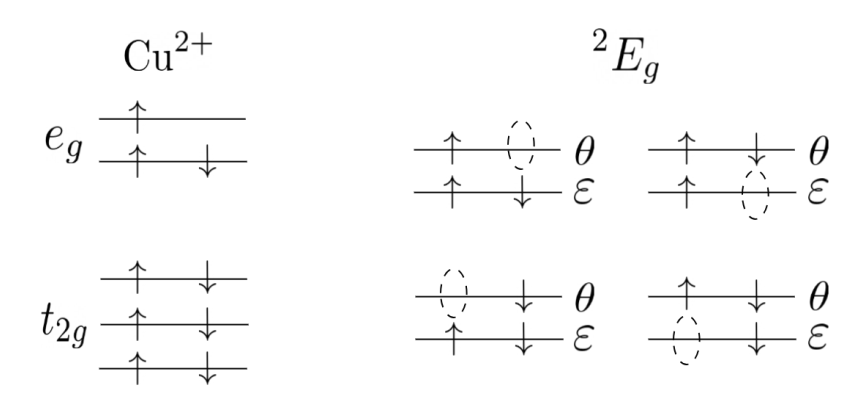


Figure 1.4: Left: Illustration of the t_{2g} and e_g energy levels in the Cu²⁺ ion. Right: All four possibilities for the last electron in the e_g orbitals.

In KCuF₃, the cooperative JTE (cJTE) not only determines the local distortions of the octahedra, but also propagates throughout the crystal, giving rise to collective structural changes [6–8]. The cJTE in KCuF₃ leads to the collective distortion of adjacent octahedra [9], which can form elongated/compressed pairs, for example (See Figure 1.5). This cooperative effect leads to intrinsic ferroelasticity, where the whole lattice can be distorted in one spontaneous deformation. In this sense, the ferroelastic behavior of KCuF₃ can be regarded as a macroscopic manifestation of the same principle that governs quantum tunneling in molecules: the existence of multiple equivalent minima, think of equivalent elongations of the crystal in each direction,

1.3. OBJECTIVES 5

in the adiabatic potential energy surface, between which the system may oscillate or switch. In real crystals, however, defects can break the symmetry and localize the system in a single minimum.

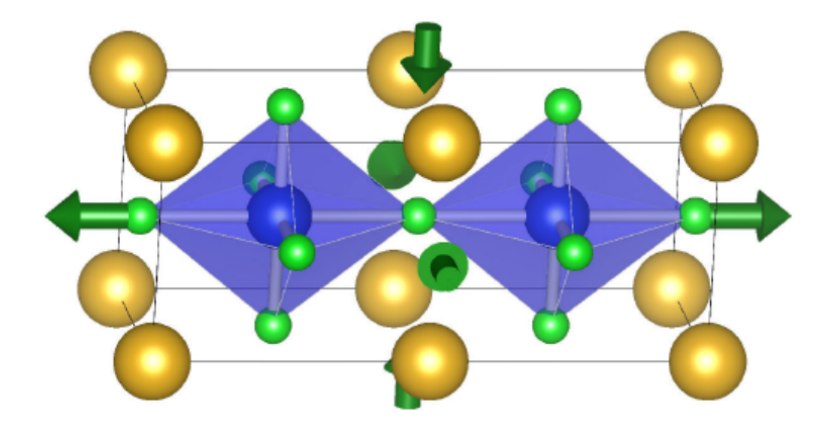


Figure 1.5: Cooperative Jahn-Teller effect in KCuF₃. Figure obtained from ref. [10]

A central question that arises is whether such tunneling processes are observable in solids. The answer depends on the tunneling frequency, that is, the energy splitting between the states associated with different lattice configurations. If the quantum effects are strong enough to prevent the system from being pinned to a single minimum by defects, the tunneling can manifest in measurable macroscopic magnitudes such as the lattice parameters or elastic constants. Thus, the study of KCuF₃ provides not only a canonical example of the cJTE but also a way to explore how local vibronic instabilities translate into collective ferroelastic properties, and whether tunneling dynamics can be detected at the macroscopic scale.

1.3 Objectives

The main goal of this work is to investigate the interplay between electronic and nuclear dynamics in systems where the Born-Oppenheimer approximation breaks down, with particular emphasis on the Jahn-Teller effect in solids. Specifically, the objectives of this study are:

- To determine the **tunneling period in a solid-state system**, namely KCuF₃. The cooperative Jahn-Teller effect in this perovskite provides a prototypical case where local vibronic instabilities can propagate through the lattice. By evaluating the tunneling frequency, we seek to assess whether such processes can be experimentally observable at the macroscopic scale, for instance in lattice parameters or elastic properties.
- To analyze the **influence of electronic motion on quantum tunneling**. The objective is to study how the coupling between electronic and nuclear motions alters the tunneling process, both in terms of the resulting energy splittings and in the possible inversion of level ordering due to topological effects such as the Berry phase.
- To develop a computational program that accounts for the simultaneous motion of electrons and nuclei. The purpose of this code is to construct model Hamiltonians that incorporate both electronic and nuclear dynamics on equal footing, allowing us to explore scenarios where the Born-Oppenheimer separation fails and to provide numerical estimates of tunneling splittings in Jahn-Teller systems.

1.4 Structure of this work

This work is divided into 5 chapters. Firstly, in this introductory chapter, we have presented the context and motivation for this study on the Jahn-Teller Effect in KCuF₃, as well as the main objectives of the research.

In the second chapter, we will delve into the theoretical framework of vibronic coupling (See Chapter 2), providing a comprehensive overview of the key concepts and mathematical formulations and derivations. In this chapter, the Hamiltonian of a non-adiabatic system will be introduced, along with the main models used to describe the vibronic interactions.

The third chapter will focus on the computational methods employed in this study (See Chapter 3). Here, we will discuss the various techniques and approaches used to study many physical problems. In particular, we will highlight the importance of first-principles methods, methods that use no other information than fundamental constants, and their role in understanding the Jahn-Teller Effect.

The fourth chapter is the core of this work (See Chapter 4). This chapter is divided into three main sections. The first section will study the theoretical behavior of non-warped and warped Jahn-Teller systems, providing a detailed analysis of the latter's tunneling dynamics. The second section will present a computational solution developed for the Jahn-Teller problem based on a finite difference method. At last, in the third section, numerical results will be discussed, comparing the theoretical predictions with the outcomes of the computational simulations.

Lastly, in the last chapter (See Chapter 5), we will summarize the main findings and conclusions of this study. We will also discuss the implications of our results and suggest potential directions for future research in this field.

Chapter 2

Vibronic Coupling Theory

In the context of quantum mechanics, the Schrödinger equation is a fundamental equation that describes the behavior of a systems in the microscopic world. In our case, we are interested in studying the coupling between the atomic vibrations and the electronic movement, the so-called *vibronic interaction* that takes place in molecular or solid-state systems. The Schrödinger equation for these problem is given by

$$\hat{H}(\mathbf{r}, \mathbf{R})\Psi(\mathbf{r}, \mathbf{R}) = E\Psi(\mathbf{r}, \mathbf{R}) \tag{2.1}$$

where \mathbf{r} denotes the set of all electronic coordinates, $\mathbf{r} = \{\vec{r}_i : i = 1, ..., n\}$, \mathbf{R} denotes the set of all nuclear coordinates, $\mathbf{R} = \{\vec{R}_{\alpha} : \alpha = 1, ..., N\}$. \hat{H} is the Hamiltonian operator and E is the energy of the eigenstate $\Psi(\mathbf{r}, \mathbf{R})$. Along this section, we will introduce the vibronic coupling theory and its implications for the Jahn-Teller effect. The reference [4] has been mainly followed for this chapter.

2.1 The Hamiltonian

The Equation (2.1) has generally no analytical solution and so we need to apply some approximate method to solve it. First, let us write the Hamiltonian operator as follows:

$$\hat{H} = \hat{T}_e + \hat{T}_n + \hat{V}_{ee} + \hat{V}_{en} + \hat{V}_{nn}, \tag{2.2}$$

$$\hat{T}_e = -\sum_{i=1}^n \frac{\hbar^2}{2m_e} \nabla_{r_i}^2, \tag{2.3}$$

$$\hat{T}_n = -\sum_{\alpha=1}^N \frac{\hbar^2}{2M_\alpha} \nabla_{R_\alpha}^2, \tag{2.4}$$

$$\hat{V}_{ee} = \frac{1}{2} \sum_{i \neq j} \frac{e^2}{|\vec{r}_i - \vec{r}_j|}, \tag{2.5}$$

$$\hat{V}_{en} = \sum_{i,\alpha} -\frac{e^2 Z_{\alpha}}{|r_i - R_{\alpha}|},\tag{2.6}$$

$$\hat{V}_{nn} = \frac{1}{2} \sum_{\alpha \neq \beta} \frac{e^2 Z_{\alpha} Z_{\beta}}{|R_{\alpha} - R_{\beta}|}$$
(2.7)

where m_e is the mass of the electron and M_{α} is the mass of the nucleus α . These terms are the electronic (Eq. (2.3)) and nuclear (Eq. (2.4)) kinetic energy operators, as well as the classic electron-electron (Eq. (2.5)), electron-nuclear (Eq. (2.6)), and nuclear-nuclear (Eq. (2.7)) Coulomb interaction potentials.

In order to study the vibronic coupling we would like to be able to use the symmetry of the system. To do so, first we need to define a reference geometry for the nuclear positions, which we will denote as \vec{R}_0 . This reference geometry is usually chosen as the geometry with highest symmetry [4]. If we recall the case of ammonia in Chapter 1, ammonia has two equivalent stable states in the shape of a pyramid (C_{3v} symmetry). We could take, for our reference configuration, the non-stable configuration in which the ammonia molecule is perfectly flat, with an equilateral triangle of hydrogen atoms and the nitrogen atom at the center of the triangle (D_{3h} symmetry). The reference configuration \vec{R}_0 is a vector in the Cartesian space \mathbb{R}^{3N} that encodes the positions of all the nuclei in this high-symmetry configuration.

We can now define a Cartesian displacement vector as $\vec{q} := \vec{R} - \vec{R}_0$. This vector \vec{q} also belongs to the space \mathbb{R}^{3N} and encodes the displacements of all the nuclei from their positions in the reference configuration, but note that some of them are redundant: this basis accounts for the three translations and three rotations (two for linear molecules) of the molecule as a whole, which do not change the internal structure of the molecule. Therefore, we can reduce the number of coordinates to 3N-6 (or 3N-5 for linear molecules) by transforming to normal mode coordinates, which are linear combinations of the Cartesian displacements that correspond to independent vibrational modes of the molecule. These normal mode coordinates are usually denoted as Q_{α} , where $\alpha=1,\ldots,3N-6$, and form a basis of the vibrational space of the molecule. If we go back to the ammonia molecule once again, the normal modes of vibration can be classified according to the irreducible representations of the D_{3h} point group. In Figure 1.1, the potential energy on the right is with respect to the movement on the z coordinate of the nitrogen, but might as well have been with respect to a Q_{A_1} vibrational coordinate, as they are equivalent for this molecule.

With this in mind, we will rewrite the Hamiltonian and group its terms by their nature:

$$\hat{H} = \hat{H}_{el} + \hat{H}_O + \hat{V}_{vib},$$
 (2.8)

$$\hat{H}_{el} = \hat{T}_e + \hat{V}_{ee} + \hat{V}_{en}^{(0)} + \hat{V}_{nn}^{(0)}, \tag{2.9}$$

$$\hat{H}_Q = \hat{T}_n, \tag{2.10}$$

$$\hat{V}_{vib} = \hat{V}_{en} - \hat{V}_{en}^{(0)} + V_{nn} - \hat{V}_{nn}^{(0)}, \tag{2.11}$$

$$\hat{V}_{en}^{(0)} = \hat{V}_{en}(\mathbf{r}, \vec{R}_0) = \hat{V}_{en}(\mathbf{r}, \mathbf{Q} = 0), \tag{2.12}$$

$$\hat{V}_{nn}^{(0)} = \hat{V}_{nn}(\vec{R}_0) = \hat{V}_{nn}(\mathbf{Q} = 0). \tag{2.13}$$

To transform the potential energy from the R_{α} coordinates to the Q_{α} coordinates, we can express it as a Taylor expansion:

$$\hat{V}_{vib}(Q) = \sum_{\alpha} \frac{\partial V}{\partial Q_{\alpha}} \bigg|_{Q=0} Q_{\alpha} + \sum_{\alpha,\beta} \frac{\partial^{2} V}{\partial Q_{\alpha} \partial Q_{\beta}} \bigg|_{Q=0} Q_{\alpha} Q_{\beta} + \dots$$
 (2.14)

2.2 Adiabatic approximation

To solve the Schrödinger Equation (2.1), that tells us about the system's dynamics, we will now introduce the adiabatic approximation. First, we will write the total wavefunction as a product of an electronic wavefunction $\varphi_k(\mathbf{r}, Q)$ and a nuclear wavefunction $\chi_k(Q)$, where k denotes the electronic state:

$$\Psi(\mathbf{r}, Q) = \sum_{k} \varphi_k(\mathbf{r}, Q) \chi_k(Q), \qquad (2.15)$$

and we will choose those electronic states $\varphi_k(\mathbf{r}, Q)$ to be the eigenstates of the electronic Hamiltonian \hat{H}_{el} .

$$(\hat{H}_{el} + \hat{V}_{vib})\varphi_k(\mathbf{r}, Q) = \varepsilon_k(Q)\varphi_k(\mathbf{r}, Q)$$
(2.16)

The adiabatic approximation is a method used to simplify the Schrödinger equation by assuming that the nuclear motion is much slower than the electronic motion, allowing electrons to adjust instantaneously to the nuclear positions. Suppose that our system is in the reference position Q=0 and that we ignore the effect of the nuclear motion over the electrons. This is equivalent to ignoring the effect of H_Q (that accounts for the kinetic energy of the nuclei) on the electronic wavefunction.

$$H_Q \varphi_k = 0 \tag{2.17}$$

We define the electronic Hamiltonian matrix elements as

$$H_{\alpha\beta} = \langle \varphi_{\alpha} | \hat{H}_{el} + \hat{V}_{vib} | \varphi_{\beta} \rangle. \tag{2.18}$$

The adiabatic approximation essentially lets us diagonalize the electronic Hamiltonian matrix $H_{\alpha\beta}$ to find the adiabatic potential energy surfaces (APES) as the eigenvalues of $H_{\alpha\beta}$.

If we substitute the total wavefunction (Eq. (2.15)) into the Schrödinger Equation (2.1), we obtain

$$(H_{el} + H_Q + \hat{V}_{vib}) \sum_{k} |\varphi_k(r)\rangle |\chi_k(Q)\rangle = E \sum_{k} |\varphi_k(r)\rangle |\chi_k(Q)\rangle$$
 (2.19)

Multiplying by $\langle \varphi_m(r)|$ and integrating, we get

$$\sum_{k} \langle \varphi_m | \left(H_e + H_Q + \hat{V}_{vib} - E \right) | \varphi_k \rangle | \chi_k(Q) \rangle = 0, \qquad (2.20)$$

$$\sum_{k} \left(\langle \varphi_m | H_{el} + \hat{V}_{vib} | \varphi_k \rangle + \langle \varphi_m | H_Q | \varphi_k \rangle - E \langle \varphi_m | \varphi_k \rangle \right) | \chi_k(Q) \rangle = 0, \tag{2.21}$$

$$\sum_{k} \left(\varepsilon_k(Q) \delta_{km} + H_Q \delta_{km} - E \delta_{km} \right) |\chi_k(Q)\rangle = 0, \tag{2.22}$$

$$(\varepsilon_k(Q) + H_O - E)|\chi_k(Q)\rangle = 0. \tag{2.23}$$

Where in Equation (2.22) we have applied the adiabatic approximation (Eq. (2.17)). And lastly, in Equation (2.23) we have obtained a Schrödinger equation for the nuclear wavefunctions. Also in Equation (2.23) the $\varepsilon_k(Q)$ is the adiabatic potential energy surface (APES) of the system.

This approximation is only valid when the separation between energy levels is sufficiently large. When the energy levels are close together, or even degenerate, the adiabatic approximation breaks down [4], and we need to go beyond it. This is the case in the Jahn-Teller systems.

2.2.1 Jahn-Teller systems

In Jahn-Teller systems, more specifically in this work, in $E \otimes e$ systems (See Chapter 1), the vibronic interaction is not negligible [4], and the adiabatic approximation is not valid. In such cases, the Schrödinger equation must be solved taking into account the vibronic interaction, therefore considering the non-diagonal terms of the Hamiltonian matrix. In a JT system, we consider the electronic states that are degenerate as the basis for Equation (2.23). The simplest case of degeneracy that we can consider is a two-fold degeneracy, as is the case for the unpaired electron in the of the Cu^{2+} ion like we discussed in Chapter 1. In the case of considering an E (doubly degenerate) state in O_h symmetry, for the first (linear) term in \hat{V}_{vib} in Equation (2.14) to be non trivial, the vibrational modes must also transform as the same irreducible representation as the electronic states.

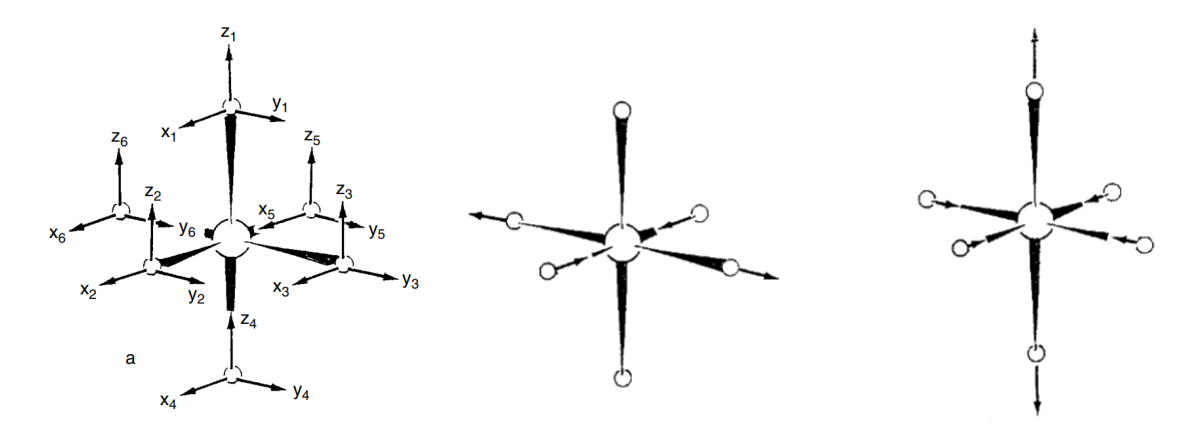


Figure 2.1: Displacements of atoms in octahedral XY₆ molecules. Left: Orthorhombic Q_{ε} displacement, Right: Tetragonal Q_{θ} displacement. Figure obtained from [4].

The two vibrational modes (See Figure 2.1) are usually denoted as θ (tetragonal distortion) and ε (orthorhombic distortion), and their respective coordinates are denoted as Q_{θ} and Q_{ε} and represent the following displacements:

$$Q_{\theta} = \frac{1}{\sqrt{12}} (2z_1 - 2z_4 - x_2 + x_5 - y_3 + y_6)$$
(2.24)

$$Q_{\varepsilon} = \frac{1}{2}(-x_3 + x_4 + y_5 - y_6) \tag{2.25}$$

(2.26)

We can then write the total wavefunction (Eq. (2.15)) as

$$\Psi(r,Q) = \varphi_{\theta}(r)\chi_{\theta}(Q_{\theta}) + \varphi_{\varepsilon}(r)\chi_{\varepsilon}(Q_{\varepsilon}). \tag{2.27}$$

And the Hamiltonian matrix in the φ_{θ} and φ_{ε} basis, $H_{\alpha\beta} = \langle \varphi_{\alpha} | \hat{H} | \varphi_{\beta} \rangle$, should then be written as

$$\hat{H} = \begin{pmatrix} \varepsilon_{\theta}(Q) + H_Q & H_{\theta\varepsilon} \\ H_{\varepsilon\theta} & \varepsilon_{\varepsilon}(Q) + H_Q \end{pmatrix}. \tag{2.28}$$

Since we expect the system to oscillate around the reference geometry, we can truncate the expansion (2.14) to the second order. We need to obtain the matrix elements of the vibronic interaction operator now. To do so, we can make use of the Wigner-Eckart theorem and the Clebsch-Gordan coefficients. This will allow us to relate the matrix elements of the vibronic interaction operator to the coupling coefficients of the vibrational modes [4]. The Wigner-Eckart theorem states that for any physical operator $X_{\overline{\Gamma}_{\overline{\gamma}}}$ that transforms as $\overline{\gamma}$ (where $\overline{\gamma}$ can be θ , ε , a_1 , a_2) of the representation $\overline{\Gamma}$ (where $\overline{\Gamma}$ here can be E, A_1 , A_2), we have

$$\langle \Gamma_{\gamma} | X_{\overline{\Gamma}_{\overline{\gamma}}} | \Gamma_{\gamma'}' \rangle = \langle \Gamma | | X_{\overline{\Gamma}} | | \Gamma' \rangle \langle \overline{\Gamma}_{\overline{\gamma}} \Gamma_{\gamma'}' | \Gamma_{\gamma} \rangle, \tag{2.29}$$

where $\langle \Gamma || X_{\overline{\Gamma}} || \Gamma' \rangle$ is the reduced matrix element and $\langle \overline{\Gamma}_{\overline{\gamma}} \Gamma'_{\gamma'} | \Gamma_{\gamma} \rangle$ is the corresponding Clebsch-Gordan coefficient in Table 2.1.

$E \times E$		A_1	A_2	E	
	Ľ	a_1	a_2	θ	ε
θ	θ	$\frac{1}{\sqrt{2}}$	•	$-\frac{1}{\sqrt{2}}$	•
ε	ε	$\frac{1}{\sqrt{2}}$		$\frac{1}{\sqrt{2}}$	
θ	ε	•	$\frac{1}{\sqrt{2}}$		$\frac{1}{\sqrt{2}}$
ε	θ	•	$-\frac{1}{\sqrt{2}}$	•	$\frac{1}{\sqrt{2}}$

Table 2.1: Clebsch-Gordan coefficients for $E \otimes e$ products for the octahedral group. [11]

The linear terms of the vibronic interaction operator are given by the columns under the E representation and the left columns tell us about the states that are being multiplied. For example, if we wanted to know the matrix element

$$\langle \varphi_{\theta} | \frac{\partial V(r, Q)}{\partial Q_{\theta}} | \varphi_{\theta} \rangle,$$
 (2.30)

we would look on the table and look for the coefficient corresponding to the θ coordinate: $-\frac{1}{\sqrt{2}}$. The same can be done for the rest of the combinations. One can easily see that the $\varepsilon\varepsilon$ element has the opposite sign to the $\theta\theta$ element and the two cross elements are zero. Therefore, the linear terms can be expressed as matrices in the following way:

$$H_{\theta}^{(1)} := \left\langle \frac{\partial H}{\partial Q_{\theta}} \right\rangle = V \begin{pmatrix} -1 & 0\\ 0 & 1 \end{pmatrix},$$
 (2.31)

$$H_{\varepsilon}^{(1)} := \left\langle \frac{\partial H}{\partial Q_{\varepsilon}} \right\rangle = V \begin{pmatrix} 0 & 1\\ 1 & 0 \end{pmatrix},$$
 (2.32)

where the constant V absorbs the $1/\sqrt{2}$ factors. These terms should be attached to Q_{θ} and Q_{ε} , respectively. For the higher order terms, instead of obtaining the coefficients that are associated with each of the higher order terms, we can use the table and obtain the higher order perturbations as follows: Instead of looking at the table by rows, we can look at it by columns, and the left-most column tells us what Q_i are being multiplied. Thus, we will obtain the coefficients associated with these vibrational modes.

$$Q_{a1}^{(2)} = \frac{1}{\sqrt{2}}(Q_{\theta}^2 + Q_{\varepsilon}^2), \tag{2.33}$$

$$Q_{a2}^{(2)} = \frac{1}{\sqrt{2}}(Q_{\theta}Q_{\varepsilon} - Q_{\varepsilon}Q_{\theta}) = 0,$$
 (2.34)

$$Q_{\theta}^{(2)} = \frac{1}{\sqrt{2}}(Q_{\varepsilon}^2 - Q_{\theta}^2),$$
 (2.35)

$$Q_{\varepsilon}^{(2)} = \frac{2}{\sqrt{2}}(Q_{\theta}Q_{\varepsilon}). \tag{2.36}$$

Following this notation, it is obvious that $Q_i^{(1)} = Q_i$, for $i = \theta, \varepsilon$. From these, we can obtain their corresponding matrix elements:

$$H_{a1}^{(2)} = K \begin{pmatrix} \frac{1}{\sqrt{2}} & 0\\ 0 & \frac{1}{\sqrt{2}} \end{pmatrix}, \tag{2.37}$$

$$H_{a2}^{(2)} = 0, (2.38)$$

$$H_{\theta}^{(2)} = 2F \begin{pmatrix} \frac{-1}{\sqrt{2}} & 0\\ 0 & \frac{1}{\sqrt{2}} \end{pmatrix},$$
 (2.39)

$$H_{\varepsilon}^{(2)} = 2F \begin{pmatrix} 0 & \frac{1}{\sqrt{2}} \\ \frac{1}{\sqrt{2}} & 0 \end{pmatrix} \tag{2.40}$$

We can therefore summarize the vibronic interaction operator using the Pauli matrices, yielding the following expression:

$$H_{vib} = E_0 - V(Q_\theta \hat{\sigma}_z - Q_\varepsilon \hat{\sigma}_x) + \frac{K}{2}(Q_\theta^2 + Q_\varepsilon^2) + F((Q_\theta^2 - Q_\varepsilon^2)\hat{\sigma}_z + 2Q_\theta Q_\varepsilon \hat{\sigma}_x), \tag{2.41}$$

where E_0 is the energy of the system at the reference position of the nuclei, the $\hat{\sigma}_0$ or identity matrix has been omitted and the Pauli matrices involved are

$$\hat{\sigma}_z = \begin{pmatrix} -1 & 0 \\ 0 & 1 \end{pmatrix}, \qquad \hat{\sigma}_x = \begin{pmatrix} 0 & 1 \\ 1 & 0 \end{pmatrix}.$$
 (2.42)

Note that this representation shows that this operator is symmetric with real valued coefficients, and therefore the eigenvalues of this operator are real. This is to be expected, since this operator represents the potential energy of the system, and therefore its eigenvalues should be the adiabatic potential energy surfaces of the system (See Eq. 2.23). Let us recall that for any symmetric 2×2 matrix of the form

$$H = \begin{pmatrix} a & b \\ b & c \end{pmatrix}, \tag{2.43}$$

there always exists a closed form solution for the eigenvalues, given by

$$\lambda_{\pm} = \frac{a + c \pm \sqrt{(a - c)^2 + 4b^2}}{2}.$$
(2.44)

Thus, we can obtain the two sheets of the potential energy surface for this model by substituting the coefficients of the vibronic interaction operator (2.41) into (2.44). The result is the following expression for the Jahn-Teller potential energy surface:

$$E_{\pm} = E_0 + \frac{K}{2}(Q_{\theta}^2 + Q_{\varepsilon}^2) \pm \sqrt{(VQ_{\theta} - F(Q_{\theta}^2 - Q_{\varepsilon}^2))^2 + (VQ_{\varepsilon} + 2FQ_{\theta}Q_{\varepsilon})^2}.$$
 (2.45)

We can change to polar coordinates, where $Q_{\theta} = \rho \cos(\phi)$ and $Q_{\varepsilon} = \rho \sin(\phi)$, and the potential energy surface can be expressed as

$$E_{\pm} = \frac{1}{2}K\rho^2 \pm \left(V^2\rho^2 + F^2\rho^4 + 2VF\rho^3\cos(3\phi)\right)^{1/2}.$$
 (2.46)

The effect of the vibronic interaction associated to the second order vibronic coupling coefficient, F, is to introduce anisotropy in the potential energy surface, that is, it introduces angle

dependence in the potential energy surface, effectively creating minima in the surface. Should we disregard this term, the potential energy surface becomes radially symmetric, i.e.,

$$E_{\pm} = E_0 + \frac{K}{2}\rho^2 \pm V\rho, \tag{2.47}$$

whose lower sheet forms a shape commonly known as Mexican hat potential (See Figure 2.2).

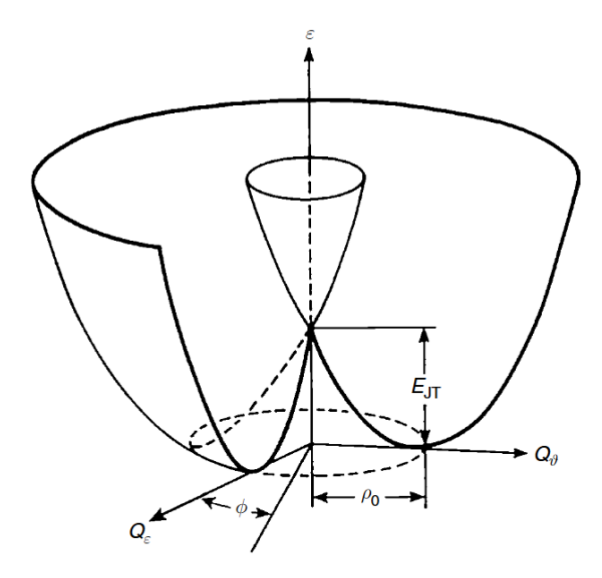


Figure 2.2: Mexican hat potential energy surface (See Eq. 2.47). Figure obtained from [4]

In this representation, the solution of the Schrödinger equation is no longer given by the $|\theta\rangle$ and $|\varepsilon\rangle$ states and their linear combination, but rather by the eigenstates that diagonalize the vibronic interaction operator, which are

$$\begin{cases} |+\rangle = \sin\left(\frac{\Omega}{2}\right)|\theta\rangle + \cos\left(\frac{\Omega}{2}\right)|\varepsilon\rangle, \\ |-\rangle = \cos\left(\frac{\Omega}{2}\right)|\theta\rangle - \sin\left(\frac{\Omega}{2}\right)|\varepsilon\rangle, \end{cases}$$
 (2.48)

where the angle Ω is related to the coefficients via the following Equation [4]:

$$\tan(\Omega) = \frac{V\sin(\phi) - K\rho\sin(2\phi)}{V\cos(\phi) + K\rho\cos(2\phi)}.$$
 (2.49)

The solution wavefunction is then given by the linear combination of these eigenstates, where the coefficients are again the nuclear wavefunctions $|\chi_{\pm}\rangle$, now in the basis of the eigenstates of the vibronic interaction operator:

$$|\Psi\rangle = |\chi_{+}\rangle|+\rangle + |\chi_{-}\rangle|-\rangle. \tag{2.50}$$

Note that when the system makes a 2π radian rotation, the electronic eigenstates, $|+\rangle$ and $|-\rangle$, change sign. This phenomenon is known as Berry phase [12]. This means that the system has a non-trivial topology, and therefore the eigenstates are not simply related to the original states $|\theta\rangle$ and $|\varepsilon\rangle$, but rather they are related to them through a non-trivial transformation, as shown in Equation (2.48). This acquisition of a Berry phase, of $\exp(i\pi) = -1$ in this case, is characteristic of JT systems and is due to the conical intersection [4] in the potential energy surface in $\rho = 0$ (See Figure 2.2).

2.2.2 Warping and higher order terms

Instead of accounting for the second order vibronic coupling term in the vibronic interaction operator as the source of anisotropy in the potential energy surface, we may consider a third order term in the expansion of the potential energy surface [13] that has been proved through first principles calculations to be very important. This term would be obtained in the same way as the ones before, resulting in the following third order term and their corresponding coupling coefficients:

$$Q_{a1}^{(3)} = -\frac{1}{2}Q_{\theta}(Q_{\theta}^2 - 3Q_{\varepsilon}^2), \qquad H_{a1}^{(3)} = -2G\begin{pmatrix} 1 & 0\\ 0 & 1 \end{pmatrix}, \tag{2.51}$$

where the -2 factor is introduced in order to cancel the -1/2 factor in the definition of the third order term, it can be seen as the coupling constant G absorbing the factors. This term is known as the elastic cubic anharmonicity and is the main term responsible for the warping of the Mexican hat surface [13]. Since the warping term, is more prominent than the second order term as proven by first principles calculations[13], we can consider only the warping term as the source of anisotropy in the potential energy surface.

$$H_{vib} = E_0 - V(Q_\theta \hat{\sigma}_z - Q_\varepsilon \hat{\sigma}_x) + \frac{K}{2}(Q_\theta^2 + Q_\varepsilon^2) + GQ_\theta(Q_\theta^2 - 3Q_\varepsilon^2), \tag{2.52}$$

Since the warping term is diagonal, it can be just added to the potential energy surface, and so we can write the potential energy surface as

$$E_{\pm} = E_0 + \frac{K}{2}(Q_{\theta}^2 + Q_{\varepsilon}^2) \pm V\sqrt{Q_{\theta}^2 + Q_{\varepsilon}^2} + GQ_{\theta}(Q_{\theta}^2 - 3Q_{\varepsilon}^2), \tag{2.53}$$

or, in polar coordinates,

$$E_{\pm} = E_0 + \frac{K}{2}\rho^2 \pm V\rho + G\rho^3 \cos(3\phi). \tag{2.54}$$

It can be seen that the warping term introduces the same kind of angular dependence as the second order vibronic term, but with a different functional form. Without warping, the potential energy surface's minima is located as a trough around the origin at a fixed radius, the warping term introduces a $2\pi/3$ periodic perturbation, which leads to a potential energy surface with three minima, which are located at the vertices of an equilateral triangle. This is because in the cubic system the x, y and z directions are equivalent, and therefore the system can elongate (or compress) in these directions equiprobably. Opposite to the minima, there are three saddle points. These are located slightly off the radius of the minima due to the warping, although they can still be considered as being at the same radius as the minima if the warping is small enough. Due to the warping, this type of potential energy surface is commonly known as tricorn hat potential (See Figure 2.3). It is easy to notice that the position of the minima and saddle points is determined by the sign of the warping term, G, and will be swapped if the sign is changed.

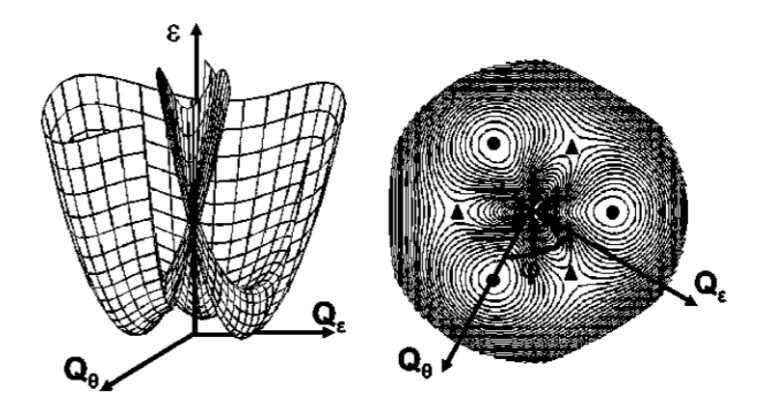


Figure 2.3: Side and top views of a tricorn hat potential energy surface. Figure obtained from [13]

Note that this model's highest order term is the third order warping term. Independent of the sign of the warping term, along the Q_{θ} axis, the potential energy surface will always grow to infinity in one direction and to minus infinity in the other. Therefore, the APES and the associated nuclear wavefunction will not necessarily be bounded if the whole Q-space is considered. It is known that these wavefunctions are bounded since the distortion is finite, and thus higher order terms seem to be important.

To ensure the boundedness of the wavefunction, an additional term will be introduced. This quartic, symmetric term must be understood as a correction to the potential energy surface, having a small coefficient, H, and just dominating in the asymptotic limit, i.e. when $Q \to \infty$, without introducing qualitative changes to the surface in the inner region. This term is given by

$$Q_{a1}^{(4)} = \frac{1}{2}(Q_{\theta}^2 + Q_{\varepsilon}^2)^2, \qquad H_{a1}^{(4)} = 2H\begin{pmatrix} 1 & 0\\ 0 & 1 \end{pmatrix}. \tag{2.55}$$

Therefore, the vibronic Hamiltonian is now given by

$$H_{vib} = E_0 - V(Q_\theta \hat{\sigma}_z - Q_\varepsilon \hat{\sigma}_x) + \frac{K}{2}(Q_\theta^2 + Q_\varepsilon^2) + GQ_\theta(Q_\theta^2 - 3Q_\varepsilon^2) + H(Q_\theta^2 + Q_\varepsilon^2)^2.$$
 (2.56)

And, once again, being a diagonal term, it can be just added to (2.54), and so we can write the potential energy surface as

$$E_{\pm} = E_0 + \frac{K}{2}(Q_{\theta}^2 + Q_{\varepsilon}^2) \pm V\sqrt{Q_{\theta}^2 + Q_{\varepsilon}^2} + GQ_{\theta}(Q_{\theta}^2 - 3Q_{\varepsilon}^2) + H(Q_{\theta}^2 + Q_{\varepsilon}^2)^2, \tag{2.57}$$

or, in polar coordinates,

$$E_{\pm} = E_0 + \frac{K}{2}\rho^2 \pm V\rho + G\rho^3 \cos(3\phi) + H\rho^4.$$
 (2.58)

This model ensures that the potential well is bounded, since, if H is sufficiently small, the quartic term will end up leading while still preserving the true shape of the well, namely, not affecting the depth and position of the minima.

Chapter 3

Computational Methods

3.1 First Principles

In order to simulate particular systems, we need precise descriptions of the APES. Equivalently, we need precise values of the vibronic coupling constants. We can obtain these values using first principles methods, which are computational methods that do not rely on empirical parameters, but rather on the fundamental laws of physics. This section has been based mainly on References [14–16].

3.1.1 Hartree-Fock

In order to solve the Schrödinger equation for a multielectronic system, let us say of N electrons, we can use the Hartree-Fock method, which is an approximation that allows us to treat the electrons as particles moving in an mean field created by the other electrons [14, 15]. Hartree's idea involved writing the many-body wavefunction $\Psi(\vec{r}_1, \ldots, \vec{r}_N)$ as the product of N single-particle molecular orbitals (MO) $\psi_i(\vec{r}_i)$, one for each electron. However, this approach neglects quantum effects such as the Pauli exclusion principle, since two electrons may have the same quantum state in this frame. Also, this approach does not treat electrons as indistinguishable particles [16]. The solution to this problem was brought by Fock, who proposed that the multielectronic wavefunction should be antisymmetrized, which can be done using a Slater determinant [14, 16]:

$$\Psi(\vec{r}_1, \dots, \vec{r}_N) = \frac{1}{\sqrt{N!}} \begin{vmatrix} \psi_1(\vec{r}_1) & \psi_2(\vec{r}_1) & \dots & \psi_N(\vec{r}_1) \\ \psi_1(\vec{r}_2) & \psi_2(\vec{r}_2) & \dots & \psi_N(\vec{r}_2) \\ \vdots & \vdots & \ddots & \vdots \\ \psi_1(\vec{r}_N) & \psi_2(\vec{r}_N) & \dots & \psi_N(\vec{r}_N) \end{vmatrix}.$$
(3.1)

This ensures that a particular electron located in a certain position cannot be associated to a certain wavefunction. Also, the Pauli exclusion principle is naturally incorporated, as the antisymmetry of the Slater determinant guarantees that if $\psi_i = \psi_j$, then $\Psi = 0$, which means that two electrons cannot occupy the same quantum state [16]. The Hartree-Fock method is an example of a variational method, which means that the system is defined by a set of variational parameters, and the solution can be reached by minimizing the energy with respect to these parameters. In this case, the variational parameters are the one-electron wavefunctions ψ_i .

To apply a variational method, we first need to obtain an expression for the energy of the system as a functional of the one-electron wavefunctions. Since our wavefunction is described with a Slater determinant, we need to obtain the energy of such a function. To do so, we can

first rewrite the Hamiltonian as

$$\hat{H} = \sum_{i=1}^{N} \hat{h} + \sum_{i=1}^{N} \sum_{j>i}^{N} \hat{g}_{ij} + V_{nn}, \tag{3.2}$$

$$\hat{h} = -\frac{1}{2}\nabla^2 - \sum_{\alpha} \frac{Z_{\alpha}}{|\vec{R}_{\alpha} - \vec{r}_i|},\tag{3.3}$$

$$\hat{g}_{ij} = \frac{1}{|\vec{r}_i - \vec{r}_j|},\tag{3.4}$$

$$V_{nn} = \frac{1}{2} \sum_{\alpha} \sum_{\beta} \frac{Z_{\alpha} Z_{\beta}}{|\vec{R}_{\alpha} - \vec{R}_{\beta}|},\tag{3.5}$$

where \hat{h} is a one-electron operator, which accounts for the kinetic energy and Coulomb attractive interaction to the nuclei of individual electrons, \hat{g}_{ij} is a two-electron operator, which accounts for the Coulomb repulsive interaction between pairs of electrons, and V_{nn} is the nuclear-nuclear Coulomb repulsive interaction. A lengthy but straightforward calculation yields the following expression for the energy of a Slater determinant (See [14], Section 3.3, for a detailed derivation):

$$E = \sum_{i=1}^{N} h_i + \frac{1}{2} \sum_{i=1}^{N} \sum_{j=1}^{N} (J_{ij} - K_{ij}) + V_{nn}.$$
 (3.6)

The J_{ij} and K_{ij} terms are the Coulomb and exchange integrals, respectively, defined as

$$J_{ij} = \int \int \frac{|\psi_i(\vec{r}_1)|^2 |\psi_j(\vec{r}_2)|^2}{|\vec{r}_1 - \vec{r}_2|} d^3 \vec{r}_1 d^3 \vec{r}_2, \tag{3.7}$$

$$K_{ij} = \int \int \frac{\psi_j^*(\vec{r}_1)\psi_i(\vec{r}_1)\psi_i^*(\vec{r}_2)\psi_j(\vec{r}_2)}{|\vec{r}_1 - \vec{r}_2|} d^3\vec{r}_1 d^3\vec{r}_2.$$
 (3.8)

Or, as operators, as

$$\hat{J}_i|\psi_j(\vec{r}_s)\rangle = \langle \psi_i(\vec{r}_t)|\hat{g}_{st}|\psi_i(\vec{r}_t)\rangle|\psi_j(\vec{r}_s)\rangle, \tag{3.9}$$

$$\hat{K}_i |\psi_i(\vec{r}_s)\rangle = \langle \psi_i(\vec{r}_t) | \hat{g}_{st} |\psi_i(\vec{r}_t)\rangle |\psi_i(\vec{r}_s)\rangle. \tag{3.10}$$

Note that the diagonal terms of the Coulomb and exchange integrals are equal, and even though the double sum in Equation 3.6 accounts for this terms, they vanish and there is no self-interaction of electrons.

On the equations above, the shape of the one-electron wavefunctions is unknown. To minimize this Slater determinant energy with respect to the shape of the MOs, the variation with respect to the shape of each MO must be zero. If we want to find a solution such that the MOs are orthonormal, this minimization must be performed under the constraint

$$\frac{\delta E}{\delta \psi_i} = 0, \forall i, \tag{3.11}$$

$$\int \psi_i^*(\vec{r})\psi_j(\vec{r})d^3\vec{r} = \delta_{ij}. \tag{3.12}$$

This constitutes a constrained optimization problem, where we need to minimize the energy functional subject to the orthonormality constraints of the MOs. This can be solved using the method of Lagrange multipliers, which results in a set of N one body equations, as opposed to the original N-electron equation. Due to being a quite technical derivation, we will not go into detail here (See [14], Section 3.3, for a detailed derivation), but the result is the following set of equations:

$$\hat{F}_i|\psi_i(\vec{r}_i)\rangle = \varepsilon_i|\psi_i(\vec{r}_i)\rangle,\tag{3.13}$$

where \hat{F}_i are the Fock operators and ε_i are the energies of the MOs.

$$\hat{F}_i = -\frac{1}{2}\nabla^2 - \sum_{\alpha} \frac{Z_{\alpha}}{|\vec{r} - \vec{R}_{\alpha}|} + \sum_{i} \frac{|\psi_i|^2}{|\vec{r} - \vec{r}_i|} = \hat{h}_i + \sum_{i=1}^{N} (\hat{J}_j - \hat{K}_j)$$
(3.14)

$$\varepsilon_i = h_i + \sum_{j=1}^{N} (J_{ij} - K_{ij}). \tag{3.15}$$

Now, electrons do not interact with each other in a one-to-one basis, but rather through the mean field created by all the electrons, therefore sometimes referred as mean-field approximation. This method usually receives the name of independent electron method as well because each electron wavefunction is the solution of the one-electron Schrödinger equation (3.13), but it must be noted that the MOs are still correlated and that electrons are not strictly independent. This method requires to know all occupied MOs in order to compute the Fock operator for a given MO, and solve for that MO. This is obviously not possible as a direct solution. However, it can be approach as an iterative process, where we start with an initial guess for the MOs and then update them until convergence is reached, therefore being called a self-consistent field (SCF) method [14].

Note that the sum of the MOs' energies ε_i is not equal to the total energy of the system [16], since they only account for the electron-nucleus interactions and the electron-mean field interactions, but does not account for the nucleus-nucleus interactions (and overcounts some of the terms). It is easy to see that the total energy can be expressed as

$$E = \sum_{i=1}^{N} \varepsilon_i - \frac{1}{2} \sum_{i,j}^{N} (J_{ij} - K_{ij}) + V_{nn}.$$
 (3.16)

3.1.2 Density Functional Theory

The Density Functional Theory (DFT) was first introduced by Hohenberg and Kohn in 1964 [17]. In their work, they proposed a method to solve the many-body problem in quantum mechanics, the electronic Schrödinger equation, by using the electron density as the fundamental variable instead of the many-body wavefunction like in Hartree-Fock. This was a significant breakthrough, as the many-body wavefunction is a complex object that depends on the coordinates of all the electrons in the system, 3N, while the electron density is a function of only three spatial coordinates. This method is based on two theorems, known as the Hohenberg-Kohn theorems [17], and the Kohn-Sham equations [18]. In this section, we will provide an overview of the key concepts and equations of DFT, the proofs and derivations can be found in [19] and [14].

Let us now delve into the details of this theory, suppose that we have a system of N electrons, whose behavior is described by the Hamiltonian

$$\hat{H} = \hat{T} + \hat{U} + \hat{V},\tag{3.17}$$

where \hat{T} is the kinetic energy operator of the electron, \hat{U} is the electron-electron interaction operator, and \hat{V} is an external potential operator, which usually accounts for the electron-nucleus interaction. Hohenberg and Kohn treat this system as an inhomogeneous electron gas, where the electron density $\rho(\vec{r})$ is the key variable. The first Hohenberg-Kohn theorem states that the external potential \hat{V} is (up to a constant) a unique functional of the electron density $\rho(\vec{r})[17, 19]$, and therefore so is the Hamiltonian and every other property of the system such

as the ground state. As a result, the ground state electron density uniquely determines all the properties of the system. If we fix the external potential $V[\rho]$ to the electron-nucleus interaction, we can write the energy functional as a functional of the electron density as follows:

$$E[\rho] = T[\rho] + E_{ee}[\rho] + E_{ne}[\rho],$$
 (3.18)

where $T[\rho]$ is the kinetic energy functional, $E_{ee}[\rho]$ is the electron-electron interaction functional, and $E_{ne}[\rho]$ is the external potential functional. Where the electronic interaction can be separated into the Coulomb and non-classical contributions, such as the exchange and correlation energies as well as the correction due to self interaction.

$$E[\rho] = T[\rho] + J[\rho] + E_{ncl}[\rho] + V_{ne}[\rho], \tag{3.19}$$

where $J[\rho]$ and $V_{ne}[\rho]$ can be obtained from the classical expressions for the Coulomb interactions in terms of the electron density:

$$J[\rho] = \frac{1}{2} \int \int \frac{\rho(\vec{r})\rho(\vec{r'})}{|\vec{r} - \vec{r'}|} d^3\vec{r} d^3\vec{r'}, \tag{3.20}$$

$$V_{ne}[\rho] = -\sum_{\alpha} \int \frac{Z_{\alpha}\rho(\vec{r})}{|\vec{R}_{\alpha} - \vec{r}|} d^3\vec{r}.$$
(3.21)

Note that the kinetic functional $T[\rho]$ and the electron-electron interaction functional $E_{ee}[\rho]$ are both universally defined functionals of the electron density, meaning that they do not depend on the specific form of the external potential $V[\rho]$. With this in mind, we can express the energy functional as

$$E[\rho] = -\sum_{\alpha} \int \frac{Z_{\alpha}\rho(\vec{r})}{|\vec{R}_{\alpha} - \vec{r}|} d^3\vec{r} + F_{HK}[\rho], \qquad (3.22)$$

where $F_{HK}[\rho]$ is the Hohenberg-Kohn functional, which encodes the universal functional dependence on the electron density:

$$F_{HK}[\rho] = T[\rho] + E_{ee}[\rho].$$
 (3.23)

Plugging in the ground state electron density $\rho_0(\vec{r})$ is sufficient to obtain all the properties of interest¹. Fortunately, the second Hohenberg-Kohn theorem is a variational theorem that guarantees that the functional that returns the energy of the ground state, $E[\rho]$ return the true ground state energy if and only if the true ground state density $\rho_0(\vec{r})$ is plugged in. Therefore, any trial density will yield an upper bound to the true ground state energy, and the equality is achieved only for the real density [17, 19]. It is clear that any trial density, as well as the true ground state density, should verify the condition $\int \rho(\vec{r})d^3\vec{r} = N$.

Even before Hohenberg's and Kohn's contribution in 1964, many other researchers had tried to formulate methods based in electron density, laying the groundwork for the development of DFT. Notable among these are the works of Thomas [20] and Fermi [21], who proposed the first methods based on constructing a functional in terms of the electron density. However, their approaches were limited and did not yield satisfactory results. Kohn and Sham [18] proposed a practical method to implement DFT. There are two terms for which the exact functional form is unknown, the kinetic energy functional $T[\rho]$ and the non-classical electron-electron interaction functional $E_{ncl}[\rho]$. Kohn and Sham proposed to treat the system as a non-interacting gas of electrons that reproduces the same electron density as the real, interacting system. This would recreate a system like that of the Hartree-Fock model, however now the Slater determinant is not an approximation to the real wavefunction, but the real solution to this non-interacting

¹This is only true for ground state properties, excited states are not directly accessible from DFT, although excited states do not give information about the distribution of the nuclei either [19].

system. The potential energy in this reference system would be a local effective potential, V_S , and the Hamiltonian would be given by

$$\hat{H}_S = -\frac{1}{2} \sum_{i=1}^N \nabla_i^2 + \sum_{i=1}^N V_S(\vec{r}_i). \tag{3.24}$$

Since the Slater determinant is the exact solution to this N-body problem, the problem can be transformed to N one-body problems, where each electron moves in the effective potential $V_S(\vec{r})$:

$$\hat{f}^{KS}\psi_i = \varepsilon_i \psi_i, \qquad \hat{f}^{KS} = -\frac{1}{2} \nabla^2 + V_S(\vec{r}), \qquad (3.25)$$

and the effective potential is such that the electron density it generates equals the true ground state density $\rho_0(\vec{r})$:

$$\rho_S(\vec{r}) = \sum_{i=1}^{N} \sum_{s} |\psi_i(\vec{r}, s)|^2 = \rho_0(\vec{r}). \tag{3.26}$$

This sum over all occupied states makes the connection to the real, interacting system. Since the kinetic energy of a non-interacting system is not equal to the real system's, the energy functional must be rewritten accordingly.

$$E[\rho] = T_S[\rho] + J[\rho] + E_{XC}[\rho] + E_{ne}[\rho], \tag{3.27}$$

where $T_S[\rho]$ is the kinetic energy functional of the non-interacting system, and $E_{XC}[\rho]$ is the exchange-correlation functional, which accounts for the difference between the real kinetic energy and the non-interacting kinetic energy, as well as the non-classical electron-electron interactions:

$$E_{XC}[\rho] = (T[\rho] - T_s[\rho]) + (E_{ee}[\rho] - J[\rho]). \tag{3.28}$$

This functional relates to the effective potential $V_S[\rho]$ through the relation:

$$V_S[\rho] = \int \frac{\rho(\vec{r'})}{|\vec{r} - \vec{r'}|} d^3 \vec{r'} + \frac{\delta E_{XC}[\rho]}{\delta \rho(\vec{r})} - \sum_{\alpha} \frac{Z_{\alpha}}{|\vec{R}_{\alpha} - \vec{r}|}.$$
 (3.29)

It is important to note that the Kohn-Sham method is exact, that is, if the functional $E_{XC}[\rho]$ were known exactly, the Kohn-Sham equations would yield the exact ground state density $\rho_0(\vec{r})$ and energy $E_0[\rho]$, since the rest of the terms are well-known. Unfortunately, to this day it is still one of the main challenges in the field of DFT to find the exact form (or better approximations) for the exchange-correlation functional. Once this functional is known, the Kohn-Sham equations can be solved self-consistently to obtain the ground state properties of the system.

3.2 CRYSTAL

CRYSTAL [22] is a computational software that implements HF and DFT methods for calculating the electronic structure of molecules and periodic systems, such as crystals. The program outputs the minimum energy configuration of a given system by optimizing an initial system. This is achieved through a self-consistent field (SCF) procedure, where the electronic density is iteratively updated until convergence is reached.

This software makes use of Gaussian-type orbitals as the basis set for the electronic wavefunctions, which allows for accurate calculations of the electronic structure. CRYSTAL has been used to create an energetic profile of KCuF₃ by computing its energy for different values of the tetragonal distortion Q_{θ} . This profile can then be used to fit the parameters of the Jahn-Teller model described in Chapter 2. 3.2. CRYSTAL 21

This program follows an iterative process to reach a minimum energy configuration. The process halts when the change in electronic density, atomic displacements, etc. between iterations are below a certain threshold, indicating that the system has reached a stable configuration. Finally, many properties of the system are output, such as the energy per unit cell, the forces on the atoms, and the electronic density.

CRYSTAL offers a fast and efficient implementation of DFT methods at the cost of not knowing the exact form of the exchange-correlation functional. Regarding this particular work, a B1WC [23] density functional was employed for the calculations. Additionally, since the program must discretize the reciprocal space, a 8x8x8 grid [24] was used to sample the Brillouin zone, that is, each directional axis in the reciprocal space was divided into 8 segments.

Chapter 4

Results

In this chapter, we will develop a computational method to solve the combined electronic-nuclear problem associated to the $E\otimes e$ problem described in Chapter 2. Firstly, we will study the behavior of JT and non-JT systems from a theoretical standpoint. Then, we will overview the finite differences method used to obtain the results presented in this chapter. Finally, results from real physical systems will be presented, showing the energy by unit cell, the tunneling splitting and the characteristic oscillation frequency and period associated to tunneling in Jahn-Teller and non-JT systems as well as the effects of Berry phase in these systems.

4.1 Nuclear dynamics in JT systems

In order to shed some light on the behavior found by the test runs, we will analyze some aspects of these systems, such as why the system is arranged doublets when no warping is introduced and why some doublets split as the warping increases, forming triplets in the extreme case. This will set the basis to analyze our more complex computational solutions.

4.1.1 Non-warped system solution

First of all, let us study the case of non-warped systems. In this scenario, the potential energy surface is symmetric and has a simple structure, which leads to the formation of doublets. To understand this, we can solve the Schrödinger equation for the system

$$-\frac{\hbar^2}{2m} \left[\frac{1}{\rho} \frac{\partial}{\partial \rho} \left(\rho \frac{\partial}{\partial \rho} \right) + \frac{1}{\rho^2} \frac{\partial^2}{\partial \phi^2} \right] |\psi\rangle + V(\rho)|\psi\rangle = E|\psi\rangle \tag{4.1}$$

where V(Q) is the potential energy surface E_{-} given by (2.47). Since the potential energy is independent of the angle ϕ , we can separate the variables and write the wavefunction as a product of two functions¹, one depending on Q and the other on ϕ :

$$|\psi(Q,\phi)\rangle = |R(Q)\rangle|\Phi(\phi)\rangle. \tag{4.2}$$

Substituting this into the Equation (4.1), and multiplying both sides by $\langle R(Q)|$, we obtain

$$\langle R|H|R\rangle|\Phi\rangle = \langle R|-\frac{\hbar^2}{2m}\left(\frac{1}{Q}\frac{\partial}{\partial Q}\left(Q\frac{\partial}{\partial Q}\right) + V(Q)\right)|R\rangle|\Phi\rangle - \frac{\hbar^2}{2m}\langle R|\frac{1}{Q^2}|R\rangle\frac{\partial^2}{\partial \phi^2}|\Phi\rangle \qquad (4.3)$$

$$=V'|\Phi\rangle - \frac{\hbar^2}{2m} \left\langle \frac{1}{Q^2} \right\rangle \frac{\partial^2}{\partial \phi^2} |\Phi\rangle = E\langle R|R\rangle |\Phi\rangle = E|\Phi\rangle, \tag{4.4}$$

¹Since the Hamiltonian is independent of the angle, it commutes with the angular momentum operator L_z , and therefore have a common base.

where $V' = \langle R| - \frac{\hbar^2}{2m} \left(\frac{1}{Q} \frac{\partial}{\partial Q} \left(Q \frac{\partial}{\partial Q}\right) + V(Q)\right) |R\rangle$ is a constant. From there, if we choose Q_0 such that $\langle 1/Q^2 \rangle = 1/Q_0^2$, we have the following equation for the angular part of the wavefunction:

$$-\frac{\hbar^2}{2mQ_0^2}\frac{\partial^2}{\partial\phi^2}|\Phi\rangle = (E - V')|\Phi\rangle. \tag{4.5}$$

This equation has a classical solution as a plane wave, that is,

$$|\Phi(\phi)\rangle = \frac{1}{\sqrt{2\pi}}e^{ik\phi}, \quad k^2 = \frac{2mQ_0^2(E - V')}{\hbar^2},$$
 (4.6)

where the multiplicative factor is a normalization constant, and the energy can be isolated as

$$E = V' + \frac{\hbar^2 k^2}{2mQ_0^2}. (4.7)$$

Lastly, our solution wavefunction must exhibit a Berry phase, and therefore fulfill the antiperiodicity condition $|\Phi(\phi + 2\pi)\rangle = -|\Phi(\phi)\rangle$, which leads to the condition $k \in \mathbb{Z} + \frac{1}{2}$, and thus having two possible values of k for every energy level, $\pm 1/2, \pm 3/2, \ldots$, which leads to the formation of doublets. Intuitively, this is because there are two possible directions of rotation around the trough, two equivalent values of angular momentum, which are degenerate in energy, and no possible solution for a non-degenerate zero angular momentum state.

Note that this term acts as a new potential energy term for the radial equation. Multiplying the original Equation (4.1) by $\langle \Phi(\phi) |$ the following equation for the radial part is obtained:

$$-\frac{\hbar^2}{2m}\left(\frac{1}{Q}\frac{\partial}{\partial Q}\left(Q\frac{\partial}{\partial Q}\right)\right)|R\rangle + \left(V(Q) + \frac{\hbar^2k^2}{2mQ^2}\right)|R\rangle = E|R\rangle, \tag{4.8}$$

where a new effective potential $V(Q) + \hbar^2 k^2/(2mQ^2)$ has been introduced. This new term pushes the radial wavefunction outwards due to the potential energy growing arbitrarily as the radius decreases, therefore is often referred to as a centrifugal potential. If anharmonic or warping terms were considered, the exact separation of variables does not hold, since the potential energy would depend on the angle as well for higher order terms [4].

4.1.2 Tunneling dynamics in JT systems

In systems with degenerate electronic states, such as the $E \otimes e$ we are focusing on, the application of the adiabatic approximation is not possible, as stated before. Nevertheless, for sufficiently great quadratic/cubic coupling constants, the system can be approximated with other techniques.

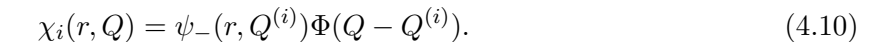
Localized quantum states

As shown in Equation (2.54), when considering the quadratic or cubic warping coefficients, the potential energy surfaces of the system are not the Mexican hat potential, but rather a tricorn potential, with 3 minima at equidistant angles. If the minima are sufficiently separated, that is, the energy barrier between them is high enough, we can consider localized states around each of the minima.

Let us assume that the system performs small oscillations around the minima. Then, low energy states, localized around the minima (See Figure 4.1), can be expressed as

$$\chi_i(r,Q) \approx \psi_-(r,Q)\Phi(Q-Q^{(i)}),\tag{4.9}$$

where $\psi_{-}(r,Q)$ is the electronic wavefunction of the lower sheet of the APES, and $\Phi(Q-Q^{(i)})$ is the vibrational wavefunction of the *i*-th potential energy well, set in the coordinates $Q^{(i)}$. Notice that this interpretation is only valid around the minima, and great displacements on Q can lead to large errors in the approximation (See Figure 4.1). Therefore, another approximation could be included, which is the use of fixed nuclear coordinates in the adiabatic function $\psi_{-}(r,Q) \approx \psi_{-}(r,Q^{(i)})$, and thus,



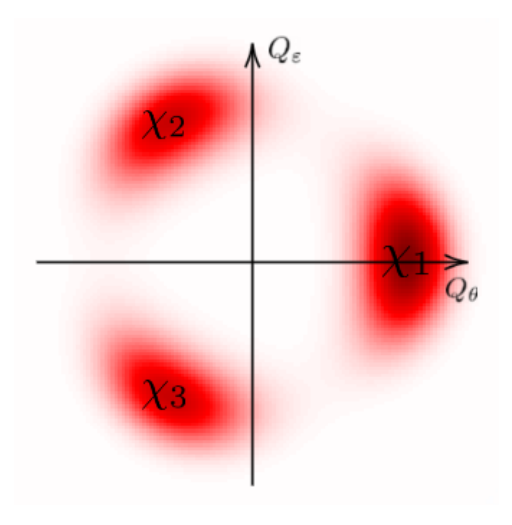


Figure 4.1: Localized states around the three minima of the tricorn potential.

Now, let us suppose that the system's stationary states can be expressed as a linear combination of the localized states. Since there are three minima, and therefore three localized states, then there must also be three stationary states. This stationary states can be written as

$$\Psi_i(r,Q) = \sum_{\alpha} c_{\alpha,i} \chi_{\alpha}(r,Q), \tag{4.11}$$

where $c_{\alpha,i}$ are the coefficients attached to the α -th localized state in the linear combination for the *i*-th stationary state. Then, these functions should satisfy the time-independent Schrödinger equation,

$$H|\Psi_i\rangle = E_i|\Psi_i\rangle,\tag{4.12}$$

where dependence on r and Q is omitted for clarity. Substituting (4.11) into the equation, the following equation is obtained:

$$H\sum_{\alpha} c_{\alpha,i} |\chi_{\alpha}\rangle = E\sum_{\alpha} c_{\alpha,i} |\chi_{\alpha}\rangle. \tag{4.13}$$

Multiplying both sides by $\langle \chi_{\beta} |$, we obtain the following system of equations, in matrix form:

$$\langle H \rangle \vec{c}_i = E \langle S \rangle \vec{c}_i, \tag{4.14}$$

Since all the localized states are equivalent, any rotation of order 3 keeps the system invariant, and so does the swapping of two of the states, thus we have some restrictions on the matrices. The equivalence of the localized states implies that the matrix elements of the form $\langle \chi_{\alpha}|H|\chi_{\alpha}\rangle$ are all equal to a constant, which we will denote as E_0 . On the other hand, the fact that the localized states are normalized implies that the matrix elements of the form $\langle \chi_{\alpha}|\chi_{\alpha}\rangle$ are all equal

to 1. For the non-diagonal elements of the two matrices, knowing the invariance under cyclic permutations of order 3 and reflections, every non-diagonal element must be equal to each other, and thus we can denote them as γ for the Hamiltonian matrix, and s for the overlap matrix, since localized states are not necessarily orthogonal. Therefore, we can write the matrices as follows:

$$\langle H \rangle = \langle \chi_{\beta} | H | \chi_{\alpha} \rangle = \begin{pmatrix} E_0 & \gamma & \gamma \\ \gamma & E_0 & \gamma \\ \gamma & \gamma & E_0 \end{pmatrix}$$

$$(4.15)$$

$$\langle S \rangle = \langle \chi_{\beta} | \chi_{\alpha} \rangle = \begin{pmatrix} 1 & s & s \\ s & 1 & s \\ s & s & 1 \end{pmatrix} \tag{4.16}$$

In these two matrices, the non-diagonal elements γ of the Hamiltonian matrix represent the tunneling energy between two localized states, the higher the value of γ , the stronger the tunneling. On the other hand, the non-diagonal elements s of the overlap matrix represent the overlap between two localized states, which is a measure of how much the two states are similar. If the minima are far apart, the overlap s will be small.

Now, this system of equations does not always have a solution, we are trying to find the vectors such that their transformation by the matrix $\langle H \rangle$ is equal to the transformation of the same vector by the matrix $E\langle S \rangle$, which is not possible for every pair of matrices.

$$(\langle H \rangle - E \langle S \rangle) \vec{c}_i = 0 \tag{4.17}$$

Nevertheless, given hermitian matrices there will be at least one solution if the kernel of the matrix $\langle H \rangle - E \langle S \rangle$ is not trivial, or in other words, if the following condition is satisfied:

$$\begin{vmatrix} E_0 - E & \gamma - Es & \gamma - Es \\ \gamma - Es & E_0 - E & \gamma - Es \\ \gamma - Es & \gamma - Es & E_0 - E \end{vmatrix} = 0.$$

$$(4.18)$$

The set of localized states follows the symmetry of the group $C_{3v} \subset O_h$, which is the symmetry group of the total system. Then, we can transform the matrix into a diagonal form, by means of the eigenvectors of the C_{3v} group, which are the following:

$$\psi_{A_1} = \frac{1}{\sqrt{3}} \begin{pmatrix} 1\\1\\1 \end{pmatrix}, \tag{4.19}$$

$$\psi_{E,1} = \frac{1}{\sqrt{6}} \begin{pmatrix} 2\\ -1\\ -1 \end{pmatrix},\tag{4.20}$$

$$\psi_{E,2} = \frac{1}{\sqrt{2}} \begin{pmatrix} 0\\1\\-1 \end{pmatrix}. \tag{4.21}$$

The eigenvectors represent the irreducible representations associated with the symmetry group of the system. There should be 3 of them, the totally symmetric representation A_1 , the antisymmetric representation A_2 and the doubly degenerate representation E. Another way of justifying this choice is via the dimension of the matrix and the irreducible representations. A_1 and A_2 are one-dimensional representations, while E is a two-dimensional representation. The matrix we are dealing with is a 3×3 matrix, and thus, the only way to represent the system is

with one E and one A-type representation, since the matrix is totally symmetric. The resulting diagonal matrix is the following:

$$\begin{pmatrix} \lambda_{A_1} & 0 & 0 \\ 0 & \lambda_E & 0 \\ 0 & 0 & \lambda_E \end{pmatrix}, \tag{4.22}$$

$$\lambda_{A_1}(E) = E_0 - E + 2\gamma - 2Es,\tag{4.23}$$

$$\lambda_E(E) = E_0 - E - \gamma + Es. \tag{4.24}$$

Since the determinant must be equal to zero, one of the eigenvalues must be equal to zero, and thus, we can find the energy levels of the system.

$$\begin{cases} \lambda_{A_1} = 0 \Rightarrow E_{A_1} = \frac{E_0 + 2\gamma}{1 + 2s} \\ \lambda_E = 0 \Rightarrow E_E = \frac{E_0 - \gamma}{1 - s} \end{cases}$$

$$(4.25)$$

The associated eigenvectors are trivially the ones in (4.19). Therefore, we have shown that with the use of the localized states, we can find the energy levels of the system if the symmetry is known, and the wells are sufficiently separated, even when the adiabatic approximation is not valid. Summarizing, these are the eigenstates of the system and their corresponding energies:

$$\Psi_{A_1} = \frac{1}{\sqrt{3}} \left(\chi_1 + \chi_2 + \chi_3 \right) \tag{4.26}$$

$$\Psi_{E,1} = \frac{1}{\sqrt{6}} \left(2\chi_1 - \chi_2 - \chi_3 \right) \tag{4.27}$$

$$\Psi_{E,2} = \frac{1}{\sqrt{2}} \left(\chi_2 - \chi_3 \right) \tag{4.28}$$

$$E_{A_1} = \frac{E_0 + 2\gamma}{1 + 2s} \tag{4.29}$$

$$E_E = \frac{E_0 - \gamma}{1 - s} \tag{4.30}$$

Tunneling Splitting

Tunneling splitting is a phenomenon that occurs in quantum systems when the energy levels of two or more states split due to the presence of a potential barrier. In the case of our study, we are considering a system with three minima, and the localized states placed around them. The three localized states are identical and thus, in the absence of interactions between the functions at the minima we would expect the ground state to be triply degenerate. However, the presence of the potential barrier between the minima and the fact that the localized states are not fully isolated leads to the two type of wavefunctions derived in the previous section: a single A_1 state and two E degenerate states. The tunneling splitting (See Figure 4.2) is the energy difference between the totally symmetric vibronic level and the doubly-degenerate vibronic level that arise when the three equivalent minima of the lower adiabatic potential surface are quantum-mechanically coupled by tunneling.

$$3\Gamma = E_{A_1} - E_E. \tag{4.31}$$

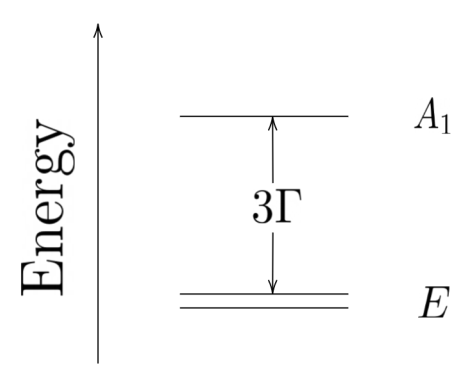


Figure 4.2: Tunneling splitting between the A_1 and E states.

Putting in the expressions for the energies, we obtain the following expression for the tunneling splitting:

$$\Gamma = \frac{\gamma - E_0 s}{1 + s - 2s^2} \tag{4.32}$$

Now, suppose that the system is set in a localized state, say χ_1 , and that the system is allowed to evolve in time. For a given state, Ψ , the system will be in a superposition of the three localized states, and the time evolution will be described by the time-dependent Schrödinger equation:

$$i\hbar \frac{\partial}{\partial t} |\Psi(t)\rangle = i\hbar \frac{\partial}{\partial t} \sum_{\alpha} c_{\alpha}(t) |\chi_{\alpha}\rangle = i\hbar \sum_{\alpha} \dot{c}_{\alpha}(t) |\chi_{\alpha}\rangle = H \sum_{\alpha} c_{\alpha}(t) |\chi_{\alpha}\rangle. \tag{4.33}$$

The problem can be simplified multiplying both sides by $\langle \chi_{\beta} |$, and solving a system of first order differential equations.

$$i\hbar \langle S \rangle \dot{\vec{c}}(t) = \langle H \rangle \vec{c}(t).$$
 (4.34)

However, a simpler approach will be given in this study. Since we do not are not looking for a general solution to the evolution of any given state, but rather the time evolution of a localized state, we can do the following. We solved the eigenstates of the Hamiltonian in terms of the localized states, so we can express the localized states in terms of the eigenstates. The localized state χ_1 is given by:

$$|\Phi\rangle(t=0) = |\chi_1\rangle = \frac{1}{\sqrt{3}}\Psi_{A_1} + \sqrt{\frac{2}{3}}\Psi_{E,1}.$$
 (4.35)

And the time evolution of the system is given by:

$$|\Phi\rangle(t) = \frac{1}{\sqrt{3}} \Psi_{A_1} e^{-iE_{A_1}t/\hbar} + \sqrt{\frac{2}{3}} \Psi_{E,1} e^{-iE_E t/\hbar}.$$
 (4.36)

From there we can compute the probability of finding the system in the initial state χ_1 as a function of time. This probability is given by

$$\mathbb{P}(\Phi(t) = \chi_1) = |\langle \chi_1 | \Phi(t) \rangle|^2 = \frac{5}{9} + \frac{4}{9} \cos\left(\frac{(E_E - E_{A_1})t}{\hbar}\right). \tag{4.37}$$

Therefore, the system will oscillate between the localized state and some mixed state and will be on the initial state with a the following frequency and period:

$$\omega = \frac{3\Gamma}{\hbar}, \qquad T = \frac{2\pi\hbar}{3\Gamma}. \tag{4.38}$$

As we have seen, what originally seemed to be a triply-degenerate system due to symmetry, is actually a system where the degeneracy is lifted by tunneling effects, leading to a single A_1 state and two E degenerate states. If the warping of the PES is strong enough, the localized states are less likely to tunnel between the minima, leading again to three equivalent states. What we see in Figure 4.4 is the continuous transition from a doubly degenerate non-warped system to a triply degenerate limit-case warped system.

4.1.3 Non-Jahn-Teller Systems

For non-Jahn-Teller systems, an analogous treatment can be applied, although the specifics of the potential energy surface and the resulting wavefunctions will differ. JT systems have the aforementioned conical intersection that endows them with their unique properties such as the Berry phase. If there was no intersection (no degeneracy in Q = 0), and therefore the APES can be described as a single surface, then, as a consequence of the JT theorem (See Ref. [4], Section 2.5), the linear terms must vanish. If there are no linear terms then the quadratic terms must be responsible for the minima (K would now be negative), and thus we can express the APES for a non-JT system as the following potential energy surface, given by Equation (4.39).

$$E(Q_{\theta}, Q_{\varepsilon}) = -\frac{1}{2}K\left(Q_{\theta}^2 + Q_{\varepsilon}^2\right) + GQ_{\theta}\left(Q_{\theta}^2 - 3Q_{\varepsilon}^2\right) + H\left(Q_{\theta}^2 + Q_{\varepsilon}^2\right)^2 \tag{4.39}$$

From there, the process is exactly the same as in the JT case. If we consider a non-warped solutions, G = 0, the potential can be described in terms of the radius exclusively, and therefore the angular part of the wavefunction contributes to the energy with the same term as Equation (4.7):

$$E = V' + \frac{\hbar^2 k^2}{2m\rho_0^2}. (4.40)$$

However, since this time the system does not acquire a geometrical phase when performing a loop around the origin, the wavefunction must fulfill the periodicity condition $|\Phi(\phi+2\pi)\rangle = |\Phi(\phi)\rangle$, which leads to the condition $k \in \mathbb{Z}$, and thus having a single ground state (k = 0) and a doubly-degenerate excited state $(k = \pm 1)$.

The solution for the warped case follows exactly the same reasoning with the localized states being affected by the warping of the potential energy surface. This results in the two energy levels discussed in the previous section, a single A_1 state and two E degenerate states, with the same expressions for the energies. The main difference with the JT case is that the energy levels are reversed. Since the ground state is now non-degenerate in the non-warped case and the system is only triply-degenerate for extreme warping, we can conclude the A_1 state is now lower than the E states even in the intermediate warped cases.

4.2 Computational Solution of the $E \otimes e$ Jahn-Teller Problem

To achieve the goal of this study, a Python script has been developed to compute the vibronic levels and wavefunctions of a Jahn-Teller system. The script is based on the finite differences method, which allows us to compute the energies and eigenstates of the system numerically.

4.2.1 Finite differences method

In order to compute the vibronic levels of a Jahn-Teller system, we need to solve the Schrödinger equation, and to do so numerically, it has to be adapted to its matrix form, which we will then discretize. Ultimately, we will obtain the wavefunctions of the system on the grid set to discretize the system.

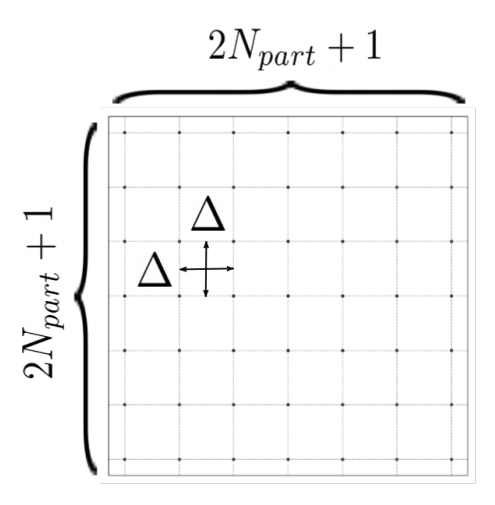


Figure 4.3: Discretization of the coordinate space into a grid of $2N_{part} + 1$ points in each coordinate. The separation between points is given by Δ .

Since our coordinate space is one generated by $\{Q_{\theta}, Q_{\varepsilon}\}$ coordinates, we will discretize the space in a grid of points. Thus, let us consider a square region of the coordinate space, such that $Q_{\theta}^{(max)} = Q_{\varepsilon}^{(max)}$, and discretize it so that there is the same number of partitions N_{part} on each side. If the point (0,0) is to be considered, this yields a total of $N = (2N_{part} + 1)^2$ cells in which we have separated this region (See Figure 4.3). Our solution wavefunction is fundamentally just an assignation of values to these N cells:

$$\psi(Q_{\theta}, Q_{\varepsilon}) = \sum_{i,j} c_{ij} \chi_{ij}(Q_{\theta}, Q_{\varepsilon}), \tag{4.41}$$

$$\chi_{ij}(Q_{\theta}, Q_{\varepsilon}) = \begin{cases} 1, & \text{if } Q_{\theta} \in (Q_{\theta}^{(i)}, Q_{\theta}^{(i+1)}), Q_{\varepsilon} \in (Q_{\varepsilon}^{(j)}, Q_{\varepsilon}^{(j+1)}), \\ 0, & \text{otherwise.} \end{cases}$$

$$(4.42)$$

If we want to solve for the complete wavefunction, we need to consider both $|\chi_{\theta}\rangle$ and $|\chi_{\varepsilon}\rangle$ components, both of them defined on this grid. Since the Hamiltonian matrix operator for each of these components is of dimension N, the total dimension of the Hamiltonian operator will be 2N.

The general method to solve problems of this kind is to write the Hamiltonian as a matrix operator and compute the operator's eigenvalues for the energies and its associated eigenvectors for the eigenstates. In order to do so, we need to discretize the Hamiltonian operator (2.28), that is, we must evaluate the Hamiltonian matrix on each point of the grid, although the kinetic energy operator should be handled with caution.

To discretize the Hamiltonian operator, we need a way to approximate the kinetic energy operator, and thus the second partial derivative operators²:

$$[T] = -\frac{\hbar^2}{2m} \left(\left[\frac{\partial^2}{\partial Q_{\theta}^2} \right] + \left[\frac{\partial^2}{\partial Q_{\varepsilon}^2} \right] \right), \tag{4.43}$$

where m is the mass of the nuclei in motion and \hbar is the reduced Planck constant. Let us check the following approximation, commonly used in the context of finite differences. If we consider a multivariable function $f(\vec{x})$ defined on a grid with spacing Δ , we approximate the second derivative with respect to x_i as

$$\frac{\partial^2 f}{\partial x_i^2}(\cdots, x_i, \cdots) = \frac{f(\cdots, x_i - \Delta, \cdots) - 2f(\cdots, x_i, \cdots) + f(\cdots, x_i + \Delta, \cdots)}{\Delta^2}, \tag{4.44}$$

²We will denote in square brackets in favor of avoiding confusion with the proper operator.

which converges to the second derivative as $\Delta \to 0$. Being Δ the step between to consecutive points on the grid (See Figure 4.3), makes it so that the result is closer to a true derivative the finer the grid is. In terms of our discretization, Equation (4.44) is represented by the following matrices:

$$[B_{\theta}] = \begin{bmatrix} -2 & 1 & 0 & \cdots & 0 \\ 1 & -2 & \ddots & & \vdots \\ 0 & \ddots & \ddots & 1 & 0 \\ \vdots & & 1 & -2 & 1 \\ 0 & \cdots & 0 & 1 & -2 \end{bmatrix}, \tag{4.45}$$

$$\left[\frac{\partial^{2}}{\partial Q_{\theta}^{2}}\right] = \frac{1}{(\Delta)^{2}} \begin{bmatrix} B_{\theta} & 0 & 0 & \cdots & 0\\ 0 & B_{\theta} & 0 & & 0\\ 0 & 0 & B_{\theta} & & 0\\ \vdots & & & \ddots & \vdots\\ 0 & 0 & 0 & \cdots & B_{\theta} \end{bmatrix},$$
(4.46)

$$\left[\frac{\partial^{2}}{\partial Q_{\theta}^{2}}\right] = \frac{1}{(\Delta)^{2}} \begin{bmatrix} B_{\theta} & 0 & 0 & \cdots & 0 \\ 0 & B_{\theta} & 0 & & 0 \\ 0 & 0 & B_{\theta} & & 0 \\ \vdots & & \ddots & \vdots \\ 0 & 0 & 0 & \cdots & B_{\theta} \end{bmatrix},$$

$$\left[\frac{\partial^{2}}{\partial Q_{\varepsilon}^{2}}\right] = \frac{1}{(\Delta)^{2}} \begin{bmatrix} -2 & \cdots & 1 & \cdots & 0 \\ \vdots & \ddots & & \ddots & \vdots \\ 1 & & -2 & & 1 \\ \vdots & \ddots & & \ddots & \vdots \\ 0 & \cdots & 1 & \cdots & -2 \end{bmatrix}.$$
(4.46)

The second derivative operator with respect to the θ coordinates can be expressed as a diagonal $(2N_{part}+1)$ -dimensional matrix where the elements along the diagonal correspond to a block $(2N_{part}+1)$ -dimensional matrix. On the other hand, the second derivative operator with respect to the ε coordinates can be expressed as a tridiagonal N-dimensional matrix, where the nonzero elements are located on the main diagonal (index 0) and the secondary diagonals of index $\pm (2N_{part}+1).$

The potential energy operator, [V], consists of a 4-block matrix of diagonal matrices. In each diagonal element of every block, corresponding to some coordinates of the Q-space, the numerical value of the potential energy is assigned, according to our model Eq. (2.56). Note that the model is a 2×2 matrix, while the numerical potential energy operator is a 2×2 -block matrix, in which the 4 values associated to the same coordinates should equal the value of the (2.56) matrix, evaluated at those coordinates. The diagonalized potential energies E_{\pm} can be obtained by substituting the 4 blocks of the operator matrix into the eigenvalue Equation (2.44), this should yield two diagonal matrices, whose elements ought to be the potential energies given by (2.58) at the corresponding coordinates, depending on the sign of the eigenvalue.

The numerical approximation to the Hamiltonian operator is then given by the sum of the kinetic and potential energy operators, that is,

$$[H] = [T] + [V]. (4.48)$$

The eigenstates and energies of the system can then be obtained by solving the eigenvalue problem. Note that the E_0 parameter is not included in the potential energy operator since the reference energy can be chosen arbitrarily³.

Essentially, the script uses a finite differences method to compute the vibronic levels of a Jahn-Teller system by discretizing the Hamiltonian operator and solving the resulting matrix

³This term only shifts the energy surface up or down, but the states' probability distributions and energies, which are relative to the ground state energy, remain unchanged.

eigenvalue problem, returning the energies of the local θ and ε vibrational modes, as well as the eigenstates of the system.

4.2.2 Program output

The developed programs need the user to input the coupling constants V (in eV/Å), K(in eV/Å²), F (in eV/Å²), G (in eV/Å³) and H (in eV/Å⁴) that characterize the APES of a given system, the mobile mass m (in atomic mass units, amu), the maximum simulation distance x_{max} (in Å), the number of partitions N_{part} and the number of selected states to be computed.

Prior to working on real systems, we will test the program with different sets of parameters, and check that the results are consistent with the theoretical predictions in the previous section. For the sake of consistency, all the test runs will be performed with the same grid, $N_{part} = 100$, mass, m = 16 amu, maximum simulation distance, $x_{max} = 1$ Å, number of selected states, 6,⁴ and quartic constant, $H = 0.001 \text{ eV/Å}^4$. The script is conceived to be as flexible as possible, and although the second order term F is neglected for this work, it is considered but set to zero.

In order to study dependence on the warping term, we will run the program with constant parameters $V=1~{\rm eV/\mathring{A}}$, $K=2~{\rm eV/\mathring{A}^2}$ and different values of the warping constant, G, while keeping the rest of the parameters constant. The results of this test are shown in Table 4.1. The energy of the first 6 vibronic levels is shown for values of G ranging from 0.00 ${\rm eV/\mathring{A}^3}$ to 0.04 ${\rm eV/\mathring{A}^3}$ in steps of 0.01 ${\rm eV/\mathring{A}^3}$. The energy levels for a warping term of $G=0.1~{\rm eV/\mathring{A}^3}$ are also shown to illustrate the convergence to the triply-degenerate limit case.

$G/\mathrm{eV}\mathring{\mathrm{A}}^{-3}$	E_0/meV	E_1/meV	E_2/meV	E_3/meV	E_4/meV	E_5/meV
0.00	0.000	0.000	1.119	1.119	3.320	3.320
0.01	0.000	0.000	0.596	1.943	3.609	3.609
0.02	0.000	0.000	0.317	2.980	4.321	4.321
0.03	0.000	0.000	0.176	4.093	5.198	5.199
0.04	0.000	0.000	0.101	5.185	6.082	6.082
0.10	0.000	0.000	0.006	$10.\bar{3}1\bar{5}$	10.453	$\bar{10.454}$

Table 4.1: Test of the warping term with different values of G. The energies are in eV, and the warping term is in eV/Å³.

The results show that for systems without warping, the states are arranged in degenerate doublets. As the warping term increases, the degeneracy is lifted for some of the states and splitting occurs, the mean energy of the states increases as well. The results of the test have been summarized in the Figure 4.4, where the energies of the states are plotted against the warping term, G.

⁴This choice may seem arbitrary, but in the previous section we have shown that these states are arranged in doublets and triplets, and it is believed that this many will be enough to show this behavior.

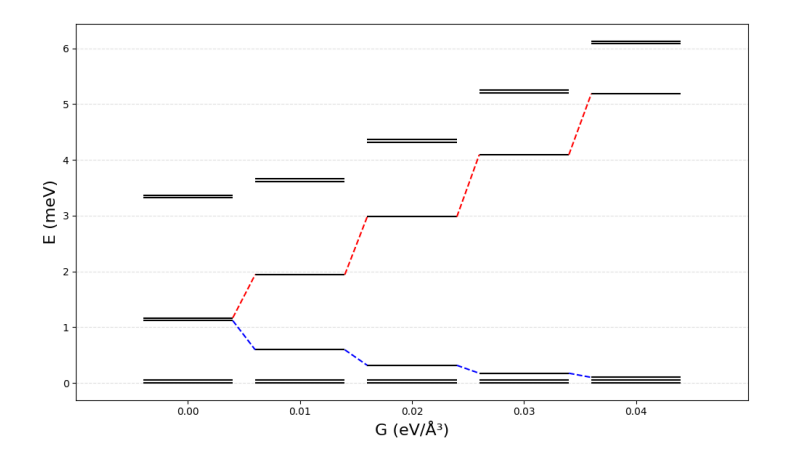


Figure 4.4: Test of the warping term with different values of G. The energies are in eV, and the warping term is in eV/Å³.

Figure 4.4 shows that the splitting of the intermediate states, E_3 and E_4 , shifts them to the ground state and the next excited state energies, respectively, as the warping term increases. Since the energy of all the states is increasing with G, convergence of the higher intermediate state to the excited level might not be as clear as the convergence of other state to the ground level. Further increasing the warping term shows that convergence is achieved in extreme cases, namely, when the warping term is very high with respect to V and K. This cannot be shown in the figure due to not being able to appreciate the energy level differences for lower values of G otherwise. The convergence of the higher intermediate state can be seen in Figure 4.4 under the dashed line, where, for $G = 0.1 \text{ eV}/\text{Å}^3$, the energy levels are almost already arranged in triplets.

4.2.3 Polar coordinates

As shown in Equation (2.56), the unwarped Mexican Hat has radial symmetry and can be nicely expressed in polar coordinates. As a consequence, one might wonder whether the program can be adapted to work with polar coordinates instead of Cartesian coordinates. From a theoretical point of view, the answer is yes, just requiring to adapt the potential and kinetic energy operators to these coordinates. Only the kinetic energy operator would need to be adapted. In polar coordinates, the kinetic energy operator is given by

$$T = -\frac{\hbar^2}{2m} \left(\frac{\partial^2}{\partial \rho^2} + \frac{1}{\rho} \frac{\partial}{\partial \rho} + \frac{1}{\rho^2} \frac{\partial^2}{\partial \phi^2} \right). \tag{4.49}$$

With this equation, the first problem that arises is that the kinetic energy operator is not well defined at the origin, $\rho=0$, since the second and third terms diverge. The coordinate transformation to polar coordinates is not well defined at the origin, and therefore, the kinetic energy operator is not well defined at the origin in polar coordinates. From a computational standpoint, this problem might not be as relevant, since we need to discretize the space in a grid, now a polar grid (See Figure 4.5), the origin can be avoided by setting a minimum distance, $\rho_{min}>0$, and the kinetic energy operator can be computed as usual.

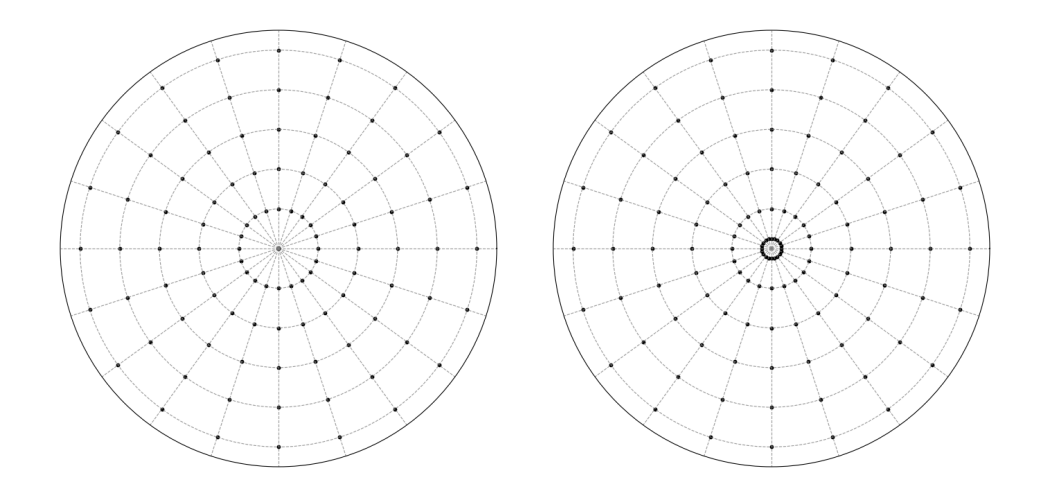


Figure 4.5: Left: Discretization in polar coordinates including the origin. Right: Discretization in polar coordinates avoiding the origin.

Another issue that arises is the hermiticity of this operator. It is clear that the kinetic energy operator is hermitian in Cartesian coordinates, but it should also be in polar coordinates. Let us check that this property still holds in polar coordinates. We say that an operator is hermitian if it satisfies the following condition:

$$\langle \psi | T\varphi \rangle = \langle T\psi | \phi \rangle, \tag{4.50}$$

with respect to the inner product in polar coordinates, defined as

$$\langle \psi | \phi \rangle = \int_0^{2\pi} \int_{\rho_{min}}^{\infty} \psi^* \phi \rho d\rho d\theta. \tag{4.51}$$

Since the kinetic energy operator is linear and, as can be seen in Equation (4.49), there are no cross derivatives, we can write the kinetic energy operator as

$$T = T_{\rho} + T_{\theta},\tag{4.52}$$

$$T_{\rho} = -\frac{\hbar^2}{2m\rho} \left(\frac{\partial}{\partial \rho} \left(\rho \frac{\partial}{\partial \rho} \right) \right), \tag{4.53}$$

$$T_{\theta} = -\frac{\hbar^2}{2m\rho^2} \frac{\partial^2}{\partial \theta^2}.$$
 (4.54)

If we prove that both T_{ρ} and T_{θ} are hermitian, then the kinetic energy operator is hermitian as well. As for the first term, we have

$$\langle \psi | T_{\rho} \phi \rangle = -\frac{\hbar^2}{2m} \int_0^{2\pi} \int_0^{\infty} \psi^* \frac{1}{\rho} \frac{\partial}{\partial \rho} \left(\rho \frac{\partial \phi}{\partial \rho} \right) \rho d\rho d\theta \tag{4.55}$$

$$=-\frac{\hbar^2}{2m}\int_0^{2\pi}\left[\psi^*\rho\frac{\partial\phi}{\partial\rho}\right]_0^\infty d\theta + \frac{\hbar^2}{2m}\int_0^{2\pi}\int_0^\infty\frac{\partial\psi^*}{\partial\rho}\rho\frac{\partial\phi}{\partial\rho}d\rho d\theta \tag{4.56}$$

$$=\frac{\hbar^2}{2m}\int_0^{2\pi}\left[\rho\frac{\partial\psi^*}{\partial\rho}\phi\right]_0^{\infty}d\theta-\frac{\hbar^2}{2m}\int_0^{2\pi}\int_0^{\infty}\frac{1}{\rho}\frac{\partial}{\partial\rho}\left(\rho\frac{\partial\psi^*}{\partial\rho}\right)\phi\rho d\rho d\theta \tag{4.57}$$

$$= -\frac{\hbar^2}{2m} \int_0^{2\pi} \int_0^{\infty} \frac{1}{\rho} \frac{\partial}{\partial \rho} \left(\rho \frac{\partial \psi^*}{\partial \rho} \right) \phi \rho d\rho d\theta = \langle T_{\rho} \psi | \phi \rangle, \tag{4.58}$$

where we have used integration by parts in the second and third equalities, and the fact that the wavefunctions vanish at the boundaries, therefore T_{ρ} is hermitian. As for the second term, by a similar argument, we have

$$\langle \psi | T_{\theta} \phi \rangle = -\frac{\hbar^2}{2m} \int_0^{2\pi} \int_0^{\infty} \psi^* \frac{1}{\rho^2} \frac{\partial^2 \phi}{\partial \theta^2} \rho d\rho d\theta \tag{4.59}$$

$$= -\frac{\hbar^2}{2m} \int_0^\infty \frac{1}{\rho} \left[\psi^* \frac{\partial \phi}{\partial \theta} \right]_0^{2\pi} d\rho + \frac{\hbar^2}{2m} \int_0^{2\pi} \int_0^\infty \frac{1}{\rho} \frac{\partial \psi^*}{\partial \theta} \frac{\partial \phi}{\partial \theta} d\rho d\theta \tag{4.60}$$

$$= \frac{\hbar^2}{2m} \int_0^\infty \frac{1}{\rho} \left[\frac{\partial \psi^*}{\partial \theta} \phi \right]_0^{2\pi} d\rho - \frac{\hbar^2}{2m} \int_0^{2\pi} \int_0^\infty \frac{1}{\rho^2} \frac{\partial^2 \psi^*}{\partial \theta^2} \phi \rho d\rho d\theta \tag{4.61}$$

$$= -\frac{\hbar^2}{2m} \int_0^\infty \left(\frac{1}{\rho^2} \frac{\partial \psi}{\partial \theta^2}\right)^* \phi \rho d\rho = \langle T_\theta \psi | \phi \rangle, \tag{4.62}$$

where we have used integration by parts in the second and third equalities again, and the fact that the wavefunctions are 2π -periodic in θ , and their derivatives as well, therefore the integral vanishes, and thus T_{θ} is hermitian as well. As a result, the kinetic energy operator is hermitian in polar coordinates, and therefore the Hamiltonian operator is hermitian as well. It can be shown that the hermiticity is conserved when discretizing the wavefunction, since it can be written as a sum of characteristic functions scaled by a constant:

$$\psi(\rho,\theta) = \sum_{i,j} c_{ij} \chi_{ij}(\rho,\theta), \tag{4.63}$$

$$\chi_{ij}(\rho,\theta) = \begin{cases} 1, & \text{if } \rho \in (\rho_i, \rho_{i+1}), \theta \in (\theta_j, \theta_{j+1}), \\ 0, & \text{otherwise.} \end{cases}$$
 (4.64)

From the theoretical standpoint, this is really nice, since the system is well behaved in polar coordinates. However, in the same way that there were no off diagonal terms for the kinetic energy in Cartesian coordinates, but the potential energy operator mixed the $|\theta\rangle$ and $|\varepsilon\rangle$ components, in this coordinate system the potential energy is diagonal, and the kinetic energy is the one that mixes the components. Moreover, while the derivative matrices are symmetric real matrices, multiplying by the $1/\rho$ and $1/\rho^2$ factors (Eq. (4.49)) leads to non symmetric matrices since matrix multiplication is not commutative, and therefore a non-hermitian operator in these coordinates. This last issue has been the main deterrent when implementing the program in polar coordinates, thus the simpler option of Cartesian coordinates has been chosen.

All of these problems do not arise in the case of Cartesian coordinates, although there are other issues that need to be addressed. The main issue is that the potential energy surface has a very important radial dependence, but in a Cartesian grid, our simulation space is a square. This could lead to a situation where a minimum distance of simulation is needed, but deep wells form in the corners, deeper that the predicted three minima (See Figure 4.6). This results in the wavefunction being spread out in the corners as a consequence of the third term growing faster than the second term and changing signs due to the cosine depending on the angle (See Eq. (2.58)). It is not a problem caused by need of more simulation distance and hence explains the reason why the quartic term is introduced.

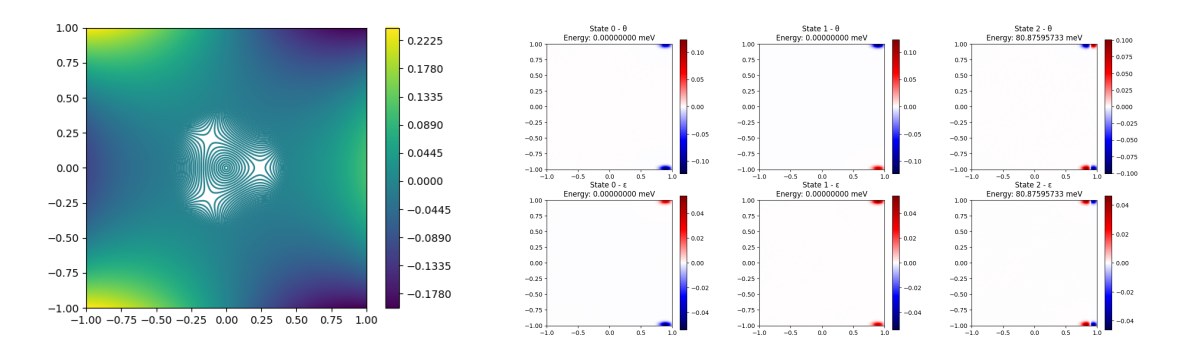


Figure 4.6: Test run corresponding to the set of fixed parameters used for Table 4.1 with $G = 3.0 \text{ eV/Å}^3$. Left: Potential energy surface with minimum values in the corners. Right: Wavefunction of the first three states of the system, showing the wavefunction being spread out in the corners.

4.3 Obtention of coupling constants and tunneling splitting

In this section, we will obtain the coupling constants of various systems with different methods. We will focus on a classical JT system, KCuF₃, for which coefficients will be obtained via simulations with CRYSTAL (See Chapter 3). In addition to this, we will also obtain the tunneling splitting of the system and the characteristic period of oscillation of a localized state in the system. Furthermore, other compounds will be considered (Triatomic molecules and impurities in crystals), although the coupling coefficients will be obtained from data previously collected in Refs. [25] and [13] instead of performing new calculations.

4.3.1 KCuF₃

In order to obtain the coupling coefficients for a KCuF₃ crystal, we will use the CRYSTAL program to perform a series of calculations that provide us with an accurate representation of the APES. Essentially, we will plot a section of the potential energy surface, along the Q_{θ} coordinate, to be precise. This axis corresponds to $Q_{\varepsilon} = 0$ in Equation (2.57). By obtaining the value for a set of energies on this surface, we can fit the parameters of the JT model.

Notice that the energy values do not show a continuous behavior, as the more central region exhibits a leap in energies (See Figure 4.8). This is due to the fact that in this crystal the Cu^{2+} ion is in a d^9 configuration, which is separated into a full t_{2g} shell (6 electrons) and an almost full e_g shell (3 electrons) (See Figure 4.7). Due to JT distortion, the energy levels split, producing a lower energy level and a higher energy level. On regular conditions, the electrons would populate the lower energy level first and then the higher energy level. However, since this is a highly symmetric cubic system, near the reference configuration, the splitting is not as high. Moreover, solids do not form well-defined energy levels, they exhibit a band structure instead. Therefore, this leads to the bands overlapping near the reference configuration, and thus, the states populating higher energy levels resulting in a metal state that is not observed in experiments (i.e. it is an artifact of the calculations).

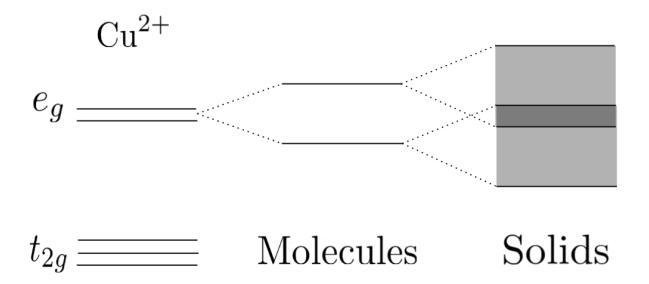


Figure 4.7: d^9 configuration of the Cu^{2+} ion in KCuF₃. The e_g is split into two bands, instead of two discrete levels.

We can fit the data corresponding to the lower sheet of the APES to the model given by Equation (2.57) with $Q_{\varepsilon} = 0$,

$$E(Q_{\theta}) = E_0 \pm VQ_{\theta} + \frac{K}{2}Q_{\theta}^2 + GQ_{\theta}^3 + HQ_{\theta}^4, \tag{4.65}$$

and obtain the values for the coupling coefficients for this solid.

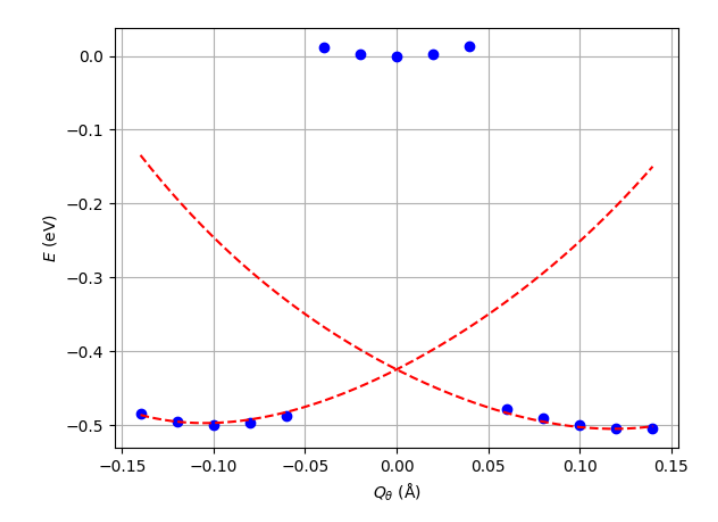


Figure 4.8: Least squares fit of the Jahn-Teller model to the KCuF₃ experimental data. Obtained parameters: $E_0 = -0.42$ eV, V = -1.26 eV/Å, K = 9.25 eV/Å², G = -2.80 eV/Å³, H = 41.67 eV/Å⁴.

In KCuF₃, the unit cell undergoes an elastic distortion that leads to the change of the lattice parameters of whole sections of the crystal. In a sense, the distortion of a unit cell pushes the atoms in the surrounding cells, therefore the mass of the unit cell has to be accounted for in the energy calculations. Plugging in the values obtained from the fit $(V = -1.26 \text{ eV/Å}, K = 9.25 \text{ eV/Å}^2, G = -2.80 \text{ eV/Å}^3, H = 41.67 \text{ eV/Å}^4)$ and the mass per unit cell of KCuF₃ (m = 159.6395 amu) into the python script, we obtain the energy density values for the KCuF₃ crystal. With the data for the first three energy levels, we can also get the value for the tunneling splitting and oscillation period of a localized state, or in other words, the oscillation period of an electron located in one of the minima of the potential energy surface. The results are shown in Table 4.2 and Figure 4.9.

Apart from the energy of the vibrational modes and the distribution of the wavefunctions, the

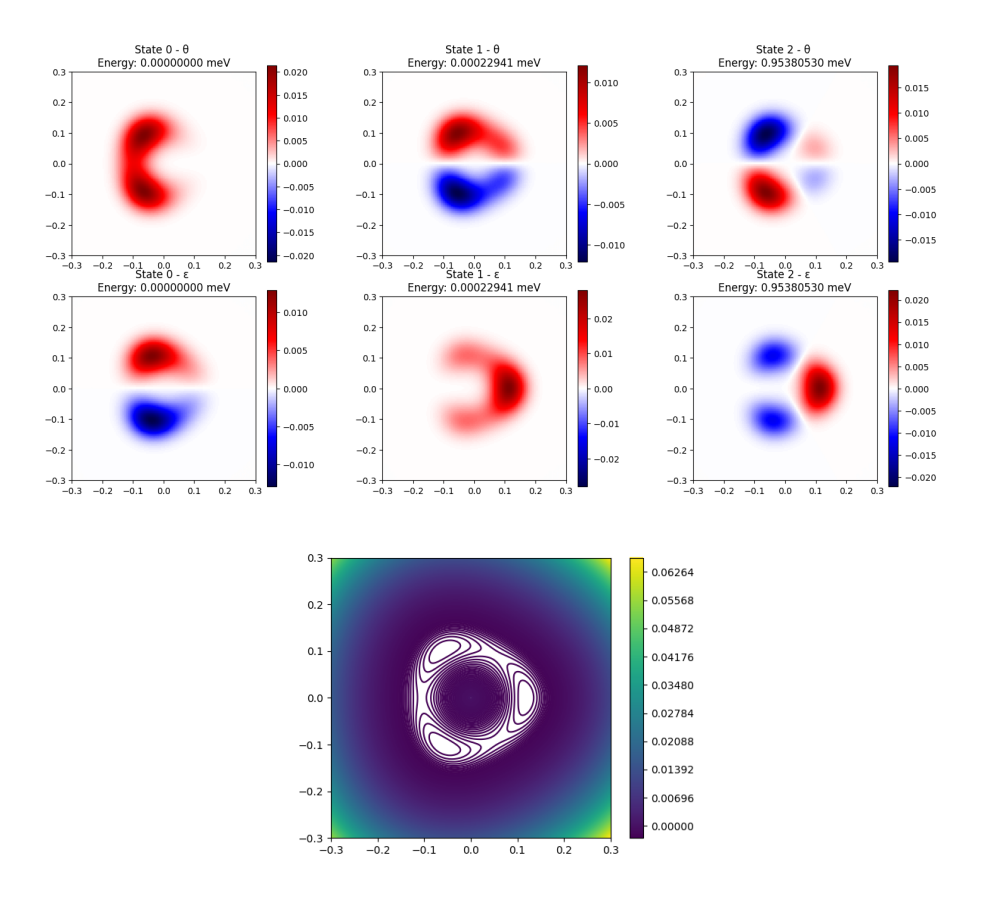


Figure 4.9: Image of the resulting wavefunctions of the first three states of the KCuF₃ crystal (top) and the corresponding APES (bottom).

vibronic Hamiltonian also plays a crucial role in determining the properties of the system. For this system, with $x_{min} = 0.3$ Å and $N_{part} = 100$, the radius of the minima is about $\rho_0 = 0.118$ Å. Keep in mind that this method is strongly dependent of the simulation distance and number of partitions chosen. A coarser grid may cause the radius to be poorly estimated.

$E^{(1)} \; (\text{meV})$	$E^{(2)} \; (\mathrm{meV})$	$3\Gamma \; (\mathrm{meV})$	$\omega \; (\mathrm{rad/ps})$	T (ps)
0.000	0.954	0.954	1.447	4.343

Table 4.2: Results for the unit cell energy of the first two excited states, tunneling splitting and angular velocity and period of oscillations in a KCuF₃ crystal. Ground state energy is not shown since energies are set relative to the ground state energy.

In addition to the energy values of the lower sheet of the APES of the system along the Q_{θ} axis, the values of the energies around the circumference defined by the minima of the potential energy surface can also be studied. This "circumference" in the Q-space is called a pseudorotation because the system is, in a sense, rotating around the center, from minimum to minimum in a periodic manner. This is not an actual rotation of the complex but rather a motion in the Q-space that produces a periodic oscillation of the distorted configurations of the system, from one distorted configuration to another [4]. The values are obtained by performing a series of calculations with the CRYSTAL program, where the angle ϕ is varied and the energy is computed for each angular value (Eq. (2.58)). As for how these values have been gathered, since CRYSTAL needs to be given the numerical values of the unit cell's parameters,

the lattice parameters in terms of the angle ϕ have been obtained beforehand. The JT distortions

only transform our system from its cubic structure in the reference position to a tetragonal or orthorrombic structure (See Figure 4.10), all three angles of the unit cell remain unchanged. Thus, only the cell constants need to be adjusted. We can think of the system as having a cubic structures with a lattice parameter $a_0 = b_0 = c_0 = R_0$. A Q_θ distortion will lead to a tetragonal structure with $a = b = R_0 - Q_\theta$ and $c = R_0 + 2Q_\theta$, according to Figure 2.1. On the other hand, a Q_ε distortion will lead to a tetragonal structure with $a = R_0 + Q_\varepsilon$, $b = R_0 - Q_\varepsilon$ and $c = R_0$, according to Figure 2.1 as well.

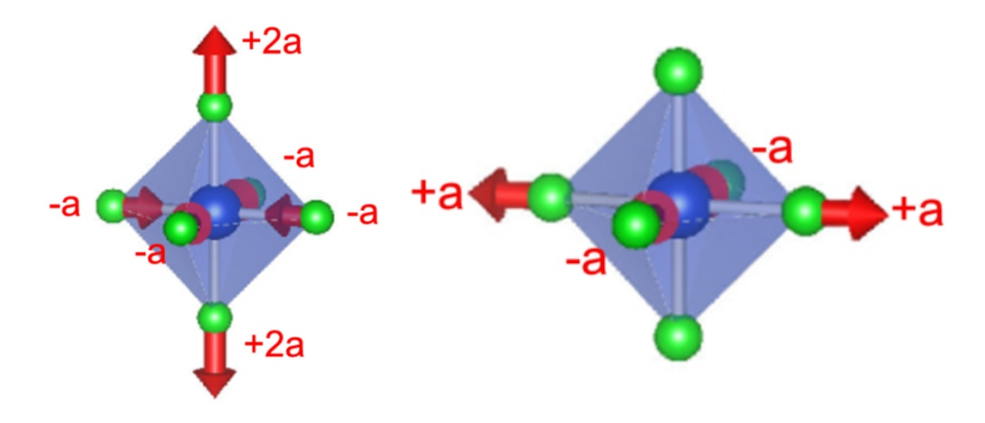


Figure 4.10: Tetragonal (Left) and orthorhombic (right) distortions of the unit cell of KCuF₃.

The path followed by a pseudorotation can then be expressed in terms of the angle ϕ as follows:

$$\begin{cases} a = R_0 - 2\sqrt{12}\alpha\cos\phi + 4\beta\sin\phi \\ b = R_0 - 2\sqrt{12}\alpha\cos\phi - 4\beta\sin\phi \\ c = R_0 + 4\sqrt{12}\alpha\cos\phi \end{cases}$$
(4.66)

Due to the system being $2\pi/3$ -periodic, the data has been gathered for the first 60 degrees, which is enough to cover the whole circumference by reflection and repetition. The data can be reflected, namely, assigning the energy value for 65° as the one for 55° , and the one for 70° as the one for 50° , and so on, until the 120° value is reached; and then extended to make the full rotation. This time, the data can be fitted to the model given by Equation (2.58) for the lower sheet setting $Q = Q_0$, the radius of the minima. This yields the simple model

$$E(\phi) = C + A\cos(3\phi),\tag{4.67}$$

where $C = E_0 + \frac{K}{2}\rho_0^2 + H\rho_0^4$ and $A = G\rho_0^3$, which are the constant to be fitted. The radius of the minima can be obtained from the fit by solving for ρ_0 in the expression for A, which is obtained numerically.

Figure 4.11 shows that the fitting is quite good, with few points deviating from the model. The reason to this discrepancy may be caused by the change of symmetry at maxima and minima that changes the accuracy of CRYSTAL solutions at these points compared to others. The maxima would correspond to the saddle points of the APES, which are not stable critical points, thus the system would spontaneously distort at these points. This time, the radius of the minima is about 0.135 Å, which is a bit higher than with the previous method.

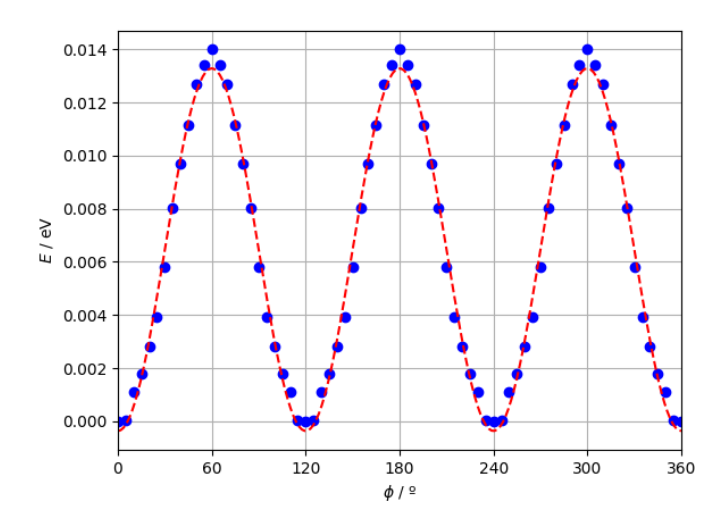


Figure 4.11: Least squares fit of the Pseudorotation model to the KCuF₃ experimental data. Obtained parameters: C = 6.46 meV, A = -6.83 meV, $Q_0 = 0.135$ Å.

Non-Jahn-Teller Approximation

Although KCuF₃ is widely known to be a prototypical example of a Jahn-Teller system, it is interesting to see how the results would change if we were to ignore the Jahn-Teller coupling in the system. This can be done by using a model that does not exhibit a conical intersection, and therefore no geometrical phase.

In order to do so, we can fit (See Figure 4.12) the experimental data obtained from the energetic profile to the model given by Equation (4.39).

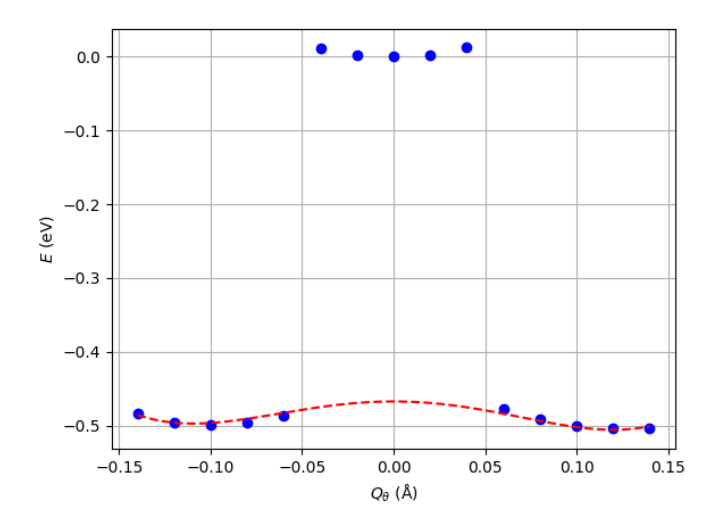


Figure 4.12: Least squares fit of the Non-Jahn-Teller model to the KCuF₃ experimental data. Obtained parameters: $E_0 = -0.47 \text{ eV}$, $K = 5.15 \text{ eV/Å}^2$, $G = -2.80 \text{ eV/Å}^3$, $H = 195.69 \text{ eV/Å}^4$.

Plugging these parameters into the model allows us to obtain the energy density values for the KCuF₃ crystal in this approximation. The results are shown in Table 4.3 and Figure 4.13.

$E^{(1)}$ / meV	$E^{(2)}$ / meV	3Γ / meV	ω / rad/ps	T / ps
1.020	1.020	1.020	1.549	4.055

Table 4.3: Results for the unit cell energy of the first two excited states, tunneling splitting and angular velocity and period of oscillations in a KCuF₃ crystal using a non-JT model. Ground state energy is not shown since energies are set relative to the ground state energy.

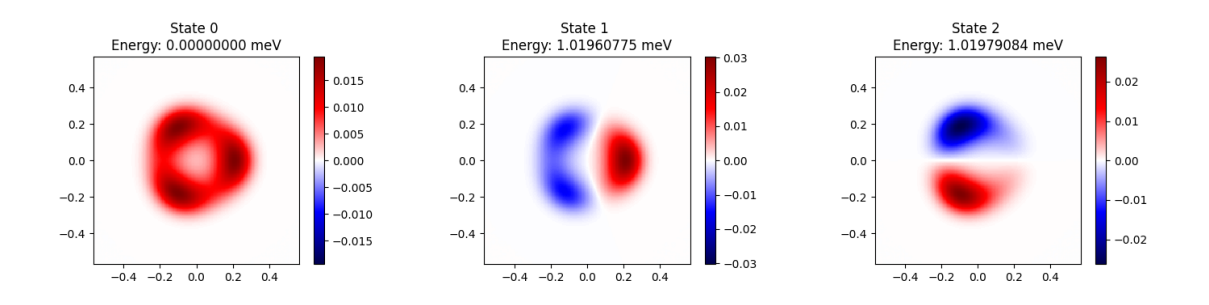


Figure 4.13: Resulting wavefunctions for the KCuF₃ crystal using a non-JT model.

From the results obtained (Table 4.3), we can see that the non-Jahn-Teller approximation shows a resemblance to the Jahn-Teller case as for the magnitude of the energy splitting, and therefore frequency and period. However, the absence of Jahn-Teller coupling in this model leads to differences in the energy levels. It is easy to see that the energy levels correspond to a degeneracy of the first excited state, as opposed to the ground state in the JT case. This is in agreement with what was expected from the theoretical analysis, since the lack of conical intersection, and therefore geometrical phase, leads to a reversal of the energy level ordering.

On the other hand, the wavefunctions obtained (Figure 4.13) might seem different to those of the Jahn-Teller case (Figure 4.9), particularly in terms of their spatial distribution. However, note that in the JT case there are two sheets of the APES, while in the non-JT case there is only one. These two sheets make it so that the total wavefunction is a linear combination of the wavefunctions from each sheet, $|+\rangle$ and $|-\rangle$. This two wavefunctions are connected to the $|\theta\rangle$ and $|\varepsilon\rangle$ electronic states by Equation (2.48). The wavefunctions shown in Figure 4.9 correspond to the wavefunctions in terms of the $|\theta\rangle$ and $|\varepsilon\rangle$ states, but if we were to transform them to their lower/upper sheets counterparts, we would obtain spatial distributions similar to Figure 4.13 for those attached to $|-\rangle$. This is in fact predicted by Equations (4.26), (4.27) and (4.28), where for both the JT and non-JT cases, the wavefunctions can be expressed in terms of the same basis states.

4.3.2 JT in impurities and molecules

The same methodology could certainly be implemented for other systems exhibiting Jahn-Teller distortions, as long as the properties of the system are comparable to those of KCuF₃, such as the presence of similar electronic configurations and local symmetries. However, in this section, we will try to obtain the same data as for KCuF₃ (Energy of the first two excited states, tunneling splitting and oscillation period) for other systems without performing CRYSTAL simulations.

Instead of relying on directly performing the calculations, where via simulations we have obtained data of the APES and fitted said data to extract the coupling coefficients of the model, we will use the data gathered in Refs. [25] and [13] to obtain the coupling coefficients and afterwards calculating the corresponding energy values. The data has been summarized in Table 4.4. In order to be consistent with other results in KCuF₃, only the data obtained

with DFT have been considered. In the original work, the coupling coefficients are named V_{1e} , V_{2a} and $V_{3}a$, they have been renamed to V, K and G to match with the used notation in this work. Table 4.4 summarizes the obtained coupling coefficients for Rh²⁺-doped NaCl, Cu²⁺- and Ag²⁺-doped MgO and CaO oxides, and Na₃, K₃, Cu₃ and Ag₃ molecules.

Compound	m / amu	V / eV/Å	K / eV/Å ²	G / eV/Å ³
NaCl:Rh ²⁺	35.45	1.17	1.93	-0.72
${ m MgO:Cu^{2+}}$	16.00	1.13	7.12	5.09
$MgO:Ag^{2+}$	16.00	1.38	10.00	11.89
CaO:Cu ²⁺	16.00	1.16	3.78	-0.96
$CaO:Ag^{2+}$	16.00	0.78	4.51	3.05
Na_3	22.99	0.44	0.52	-0.24
K_3	39.10	0.28	0.26	-0.09
Cu_3	63.55	1.07	5.10	-6.23
Ag_3	107.87	0.87	2.61	-2.14

Table 4.4: Data for the coupling coefficients of various oxides and molecular systems. Data extracted from Refs. [13, 25]. The masses of the moving nuclei are also included.

These values do not offer the complete set of coupling coefficients for the model constructed, it lacks the limiter fourth-order coefficient H. Plugging in these values directly into the program, setting H=0, does not yield accurate results. Since the system is not necessarily bounded due to fourth-order term being zero, many of these systems will not converge when the simulation box is large. A clear indication of this behavior for this is finding the wavefunctions spread out in the corners of the simulation box, and if doing a series of simulations with increasing box size, the energy values become more negative with each iteration. One could not directly rule out a simulation just by looking at the energies or the wavefunctions being spread out, since the real minima could be located out of the simulation box, but performing successive simulation might give the insight needed to identify the issue. The simulation will yield good results as long as the warping coefficient is small enough. However, many of the warping coefficients are comparable to the harmonic coefficients, which leads to the system not converging most of the times. In order to avoid this issue, it is crucial to include the fourth-order term H in the model.

Obtaining H from available data

As can be seen in Table 4.4, the data does not include an estimation for H. Thus, we will try to find a reasonable one here. One first approach is to just try to estimate the value of H numerically, by performing a series of simulations with different values of H and finding the smallest for which the minima are not located on the sides of the simulation box (an indication of non-convergence). The trial values for H ran from 0 up to 40, with increments of 0.05. This method did not give satisfactory results, some of the runs did not converge, even for large values of H, while other runs converged when H was big enough to strongly perturb the shape of the APES.

Another approach is to use a more refined and delicate criterion. For example, taking the equation that gives us the model (Eq. (2.58)), we can take the derivative on ρ and set it to zero. This results in a cubic polynomial, therefore there must be at most 3 solutions. We know that one of them is the real minimum $\rho = \rho_0$, so we can factor a $(\rho - \rho_0)$ out of the polynomial, leaving us with a quadratic equation that can be managed more easily:

$$0 = -V + K\rho + 3G\rho^2 + 4H\rho^3 = a(\rho - \rho_0)(\rho^2 + b\rho + c). \tag{4.68}$$

By performing a simple euclidean division, we find that a = 4H, $b = 4H\rho_0 + 3G$ and $c = 4H\rho_0^2 + 3G\rho_0 + K$. And from there, the two other solutions to the equation, in terms of the first, are the solution to the resulting second degree polynomial:

$$\rho_{\pm}' = \frac{-4H\rho_0 - 3G \pm \sqrt{9G^2 - 48H^2\rho_0^2 - 16KH}}{8H}.$$
(4.69)

Ideally, we would like to find H such that ρ'_{\pm} are not real numbers, therefore leaving only one solution. This approach, although mathematically sound, is numerically very unstable, and thus not really promising. Another way is thinking of H as a perturbation of some kind. In order to relate this parameter to the other coefficients, or at least to some of them, we can do the following: first we need to find the two critical points, ρ_1 and ρ_2 with $|\rho_1| < |\rho_2|$, of the APES on the positive Q_{θ} axis by differentiating and setting to zero,

$$-V + K\rho + 3G\rho^2 = 0. (4.70)$$

Then, we will choose H such that it satisfies the condition

$$3G\rho_2^2 + 4H\rho_2^3 = 0, (4.71)$$

and as a result we obtain

$$H = -\frac{3G}{4\rho_2}. (4.72)$$

This condition may seem arbitrary, but it originates from considering both G and H as perturbations of the system, this will be tackled in more detail in the following sections. The results produced with this method are collected in the Table 4.5.

Crystal	V / eV/Å	K / eV/Å ²	G / eV/Å 3	H / eV/Å 4
NaCl:Rh ²⁺	1.17	1.93	-0.72	0.41
${ m MgO:Cu^{2+}}$	1.13	7.12	5.09	-6.46
$MgO:Ag^{2+}$	1.38	10.00	11.89	-23.36
$\mathrm{CaO}:\mathrm{Cu}^{2+}$	1.16	3.78	-0.96	0.88
$CaO:Ag^{2+}$	0.78	4.51	3.05	-3.64
Na_3	0.44	0.52	-0.24	0.15
K_3	0.28	0.26	-0.09	0.04
Cu_3	1.07	5.10	-6.23	11.35
Ag_3	0.87	2.61	-2.14	2.57

Table 4.5: Data from Table 4.4 along with the derived H coefficients from Equation 4.72.

It is easy to spot the issue with these derived values: some of them are negative, and the system is not necessarily bounded. However, this is caused due to H having the opposite sign to G, and because we chose the positive Q_{θ} axis to derive the values. The negative axis could have been chosen instead. Recall that the sign of G determines if the minimum is on the positive axis G < 0 or negative G > 0 axis. Taking absolute values would account for this discrepancy and solve the issue. The energies have been calculated using these values, and they have been collected in Table 4.6.

These values may look promising, despite the disparity between some of the compounds, since the oscillation periods are in the order of picoseconds (as in the case of $KCuF_3$) and nanoseconds (a usual timescale for nuclear motions). However, they need to be consistent with the data before applying the perturbation from which the H term has been obtained (Eq. (4.72)), that is, keeping the radius of the minima near the original value. Unfortunately, numerically calculating these radii gives values two to three times larger than the original ones. Therefore, this results should be disregarded.

Crystal	$E^{(1)} \; (\mathrm{meV})$	$E^{(2)} \; (\mathrm{meV})$	$3\Gamma~({\rm meV})$	ω (THz)	T (ps)
NaCl:Rh ²⁺	0.003	0.003	0.003	0.004	1650
MgO:Cu ²⁺	0.001	1.849	1.849	2.809	2.237
$MgO:Ag^{2+}$	0.001	2.124	2.124	3.228	1.947
CaO:Cu ²⁺	0.000	0.047	0.047	0.071	88.732
$CaO:Ag^{2+}$	0.002	1.695	1.695	2.575	2.440
Na_3	0.001	0.001	0.001	0.001	5865
K_3	0.001	0.001	0.001	0.001	6488
Cu_3	0.001	0.001	0.001	0.001	5937
Ag_3	0.002	0.002	0.001	0.002	2674

Table 4.6: Results for the unit cell energy of the first two excited states, tunneling splitting and angular velocity and period of oscillations in some crystal systems. Ground state energy is not shown since energies are set relative to the ground state energy.

Approach by Interpolation

One could be tempted to obtain the coupling coefficients from a direct method at this point, in the same way as it was done for KCuF₃. However, we can try to reobtain them from existing data. We would need to find a method to obtain all of them, instead of criteria to add H from the others. Table 4.7 shows the radius of the two local minima of the APES along the Q_{θ} axis, for the extended configuration a = b < c and the contracted configuration a = b > c, along with the energy drop for those configurations for the crystal systems listed before.

Compound	Q_e (Å)	E_e (eV)	Q_c (Å)	E_c (eV)
NaCl:Rh ²⁺	0.321	0.227	0.230	0.164
${ m MgO:Cu^{2+}}$	0.080	0.035	0.008	0.039
$MgO:Ag^{2+}$	0.069	0.045	0.069	0.053
CaO:Cu ²⁺	0.118	0.038	0.107	0.032
$CaO:Ag^{2+}$	0.087	0.032	0.087	0.031
SrO:Cu ²⁺	0.146	0.047	0.159	0.035
$SrO:Ag^{2+}$	NC	NC	0.173	0.136
Na_3	0.86	$1.783 \cdot 10^{-5}$	0.33	$1.079 \cdot 10^{-5}$
K_3	0.85	$1.266 \cdot 10^{-5}$	0.42	$9.99 \cdot 10^{-6}$
Cu_3	0.15	$8.679 \cdot 10^{-6}$	0.09	$5.94 \cdot 10^{-6}$
Ag_3	0.27	$1.196 \cdot 10^{-5}$	0.14	$7.699 \cdot 10^{-6}$

Table 4.7: Data for the distance to the minima for extended and contracted tetragonal distortions in a number of JT impurities and molecules and their energy. NC stands for "Not Converging".

The problem at hand is how to recover the coefficients, which characterize the curve of the APES, from a few points on said curve. This can be achieved if we relate the minima to the energy drops with the equations of the model (2.57) with $Q_{\varepsilon} = 0$. Since they are minima, they must also be solutions to the equation given by the derivative set to zero, $\frac{\partial E}{\partial Q_{\theta}}\Big|_{Q_{\theta}=Q_{e},Q_{\varepsilon}=0} = \frac{\partial E}{\partial Q_{\theta}}\Big|_{Q_{\theta}=Q_{e},Q_{\varepsilon}=0}$

 $\frac{\partial E}{\partial Q_{\theta}}\Big|_{Q_{\theta}=Q_{c},Q_{\varepsilon}=0}=0$. This leaves a system of four equations with four unknowns⁵:

 $^{^{5}}$ The E_{0} term is just zero, since the energy drop is in relation to the reference distortion.

$$\begin{cases} E_e = -VQ_e + \frac{K}{2}Q_e^2 + GQ_e^3 + HQ_e^4, \\ E_c = VQ_c + \frac{K}{2}Q_c^2 + GQ_c^3 + HQ_c^4, \\ 0 = -V + KQ_e + 3GQ_e^2 + 4HQ_e^3, \\ 0 = V + KQ_c + 3GQ_c^2 + 4HQ_c^3. \end{cases}$$

$$(4.73)$$

Solving this system of equations gives the values for the coupling coefficients shown in Table 4.8⁶.

Crystal	$V~({\rm eV/\AA})$	$K~({\rm eV/\AA^2})$	$G~({\rm eV/\AA^3})$	$H~({\rm eV/\AA^4})$
NaCl:Rh ²⁺	3.309	36.976	7.486	-89.479
${ m MgO:Cu^{2+}}$	-9.248	-956.089	$7.889 \cdot 10^3$	$-4.112 \cdot 10^4$
$MgO:Ag^{2+}$	$1.418 \cdot 10^{15}$	$6.167 \cdot 10^{16}$	0	$-2.16 \cdot 10^{18}$
$\mathrm{CaO}:\mathrm{Cu}^{2+}$	-0.266	3.943	2.179	-125.159
$CaO:Ag^{2+}$	$1.084 \cdot 10^{14}$	$3.739 \cdot 10^{15}$	0	$-8.23 \cdot 10^{16}$
$SrO:Cu^{2+}$	-1.664	-25.645	1.7249	158.259
$SrO:Ag^{2+}$				
Na_3	$-4.674 \cdot 10^{-5}$	$1.374 \cdot 10^{-3}$	$-1.675 \cdot 10^{-3}$	$9.779 \cdot 10^{-4}$
K_3	$-1.052 \cdot 10^{-5}$	$5.643 \cdot 10^{-4}$	$-6.251 \cdot 10^{-4}$	$3.520 \cdot 10^{-4}$
Cu_3	$-1.919 \cdot 10^{-5}$	$7.192 \cdot 10^{-3}$	$-4.022 \cdot 10^{-2}$	0.120
Ag_3	$-2.554 \cdot 10^{-5}$	$3.999 \cdot 10^{-3}$	$-1.343 \cdot 10^{-2}$	0.023

Table 4.8: Coupling coefficients for the different structures obtained from solving system of equations (4.73).

These results also show some issues with the numerical values. In particular, half of the quartic coefficients are negative. Additionally, some of the coefficients are really large, which is not expected for any real physical system. This method gives results that match the original data, at the cost of possibly introducing some unphysical values. Let us think of this method in an analogous way to an interpolation. Given a set of points on the APES, we can find a polynomial, or in this case two related polynomials, that pass through those points. However, there is no way of ensuring that the quartic coefficient is positive, or that any of the coefficients explode⁷. This is therefore not a reliable method, once again. Energy values have been calculated for SrO:Cu²⁺, Na₃, K₃, Cu₃, and Ag₃, which are the only systems that showed reasonable results. This data has been gathered in Table 4.9.

Crystal	$E^{(1)} \; (\mathrm{meV})$	$E^{(2)} \; (\mathrm{meV})$	$3\Gamma \; (eV)$	ω (THz)	T (ps)
SrO:Cu ²⁺	0.013	0.883	0.001	1.342	4.681
Na_3	0.002	0.778	0.001	1.182	5.316
K_3	0.000	0.444	0.0004	0.675	9.315
Cu_3	0.000	1.515	0.0015	2.302	2.729
Ag_3	0.000	0.567	0.0006	0.862	7.290

Table 4.9: Results for the unit cell energy of the first two excited states, tunneling splitting and angular velocity and period of oscillations in some crystal systems. Ground state energy is not shown since energies are set relative to the ground state energy.

 $^{^6}$ The coupling coefficients for SrO:Ag²⁺ have not been calculated because the original data lacked information about the extended configuration.

⁷Values in the order of 10^{15} or 10^{16} are commonly labeled as numerical overflow, same as values in the order of 10^{-15} being a numerical zero or underflow, due to operations to them lose significative value.

This time, the results are more consistent with what was expected, the ones that could be worked on at least. All the oscillation periods are in the order of picoseconds, which is the same scale as the one for KCuF₃. The energy values for the ground state doublet seem to be close, which suggests that the approximations are good (There should be two degenerate ground states, this may not happen due to numerical approximations, but the energy difference should still be as low as possible). Nevertheless, not all systems could be analyzed with this method, therefore the search for a more reliable approach continues.

Approach by Correction

The last proposed method consists of using the data of Table 4.7 to construct a Mexican hat-like model and then get the warping from applying a perturbation to the model. The idea is to start with a simple double quadratic model, given by the equation:

$$E(Q) = \pm VQ + \frac{K}{2}Q^2. (4.74)$$

This model has two minima, which, ideally, should correspond to the two minima in Table 4.7, Q_e and Q_c . However, this model is symmetric with respect to the Q=0 axis, therefore the two minima are located at equal distances from the origin. We are going to consider that distance to be the mean value of the two minima, $Q_0 = \frac{Q_e + Q_c}{2}$. The energy drop for those positions should be the mean value of the two energy drops, $E_0 = \frac{E_e + E_c}{2}$. This gives two conditions to be satisfied:

$$E_0 = E(Q_0) = E(-Q_0), (4.75)$$

$$0 = \frac{\partial E}{\partial Q}(Q_0) = \frac{\partial E}{\partial Q}(-Q_0). \tag{4.76}$$

On the other hand, the warping can be introduced with a perturbation of the form

$$E'(Q) = GQ^3 + HQ^4, (4.77)$$

which is the same perturbation we used before. This perturbation breaks the symmetry of the model and introduces warping, moving one of the minima downwards and the other upwards (See Figure 4.14). Note also that changing the sign of G acts like a reflection with respect to the Q=0 axis, then if $G\to -G$, then $E'(Q)\to E'(-Q)$, and the minima are swapped. Therefore, we can assume that the deeper minima is located at $Q_0>0$ just for calculation purposes, and choose the sign of G accordingly. One can easily show that this choice ensures that $\partial^2 E'/\partial Q^2>0$ at Q_0 . The perturbation will unavoidably shift the position of the minima, but the overall shape of the potential will remain similar.

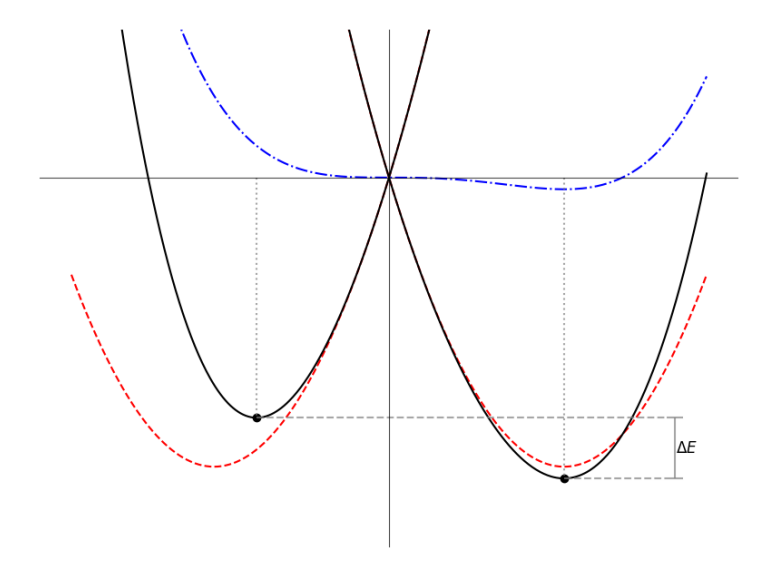


Figure 4.14: Diagram of the idea to obtain the coupling coefficients from the minima of the APES. It illustrates in red the base symmetric model, in blue the perturbation and in black the final model as the sum of both.

In order to obtain the coupling coefficients, we just need to solve the system of equations given by the base model and the perturbation, and their derivatives at the minima. For the perturbation, the condition imposed is that the difference of energies at the minima is equal to the difference of energy drops. This gives us the following system of equations:

$$-E_0 = -VQ_0 + \frac{K}{2}Q_0^2, (4.78)$$

$$0 = -V + KQ_0, (4.79)$$

$$\Delta E = E(-Q_0) - E(Q_0) = -2GQ_0^3, \tag{4.80}$$

$$0 = 3GQ_0^2 + 4HQ_0^3. (4.81)$$

Solving this system of equations will give us the values of the coupling coefficients V, K, G, and H:

$$V = \frac{2E_0}{Q_0},\tag{4.82}$$

$$K = \frac{2\Delta E}{Q_0^2},\tag{4.83}$$

$$G = \frac{E_e - E_c}{2Q_0^3},\tag{4.84}$$

$$H = -\frac{3G}{4Q_0}. (4.85)$$

Substituting the data in Table 4.7 into these equations gives the results shown in Table 4.10.

Final Results

Plugging the values from Table 4.10 into the python script resulted in the energy values, tunneling splitting and oscillation period of a localized state for these crystal systems, which are presented in Table 4.11.

All of the results seem to correspond well to what is expected for dynamics of Jahn-Teller systems. For starters, there is a good separation of energy levels, between the degenerate ground

Crystal	$V~({\rm eV/\AA})$	$K~({\rm eV/\AA^2})$	$G (eV/Å^3)$	$H~({\rm eV/\AA^4})$
NaCl:Rh ²⁺	1.4189	5.1503	-1.515	4.124
$MgO:Cu^{2+}$	1.6822	38.2317	25.470	434.154
$MgO:Ag^{2+}$	1.4213	20.5984	11.133	121.016
CaO:Cu ²⁺	0.6238	5.5446	-2.177	14.513
$CaO:Ag^{2+}$	0.7225	8.3047	-0.847	7.304
SrO:Cu ²⁺	0.5341	3.5025	-1.730	8.510
$SrO:Ag^{2+}$	1.5766	9.1135	13.170	57.095
Na_3	0.3879	0.6519	$-1.672 \cdot 10^{-5}$	$2.107 \cdot 10^{-5}$
K_3	0.2877	0.4531	$-5.205 \cdot 10^{-6}$	$6.148 \cdot 10^{-6}$
Cu_3	0.9825	8.1875	$-7.928 \cdot 10^{-4}$	$4.955 \cdot 10^{-3}$
Ag_3	0.7737	3.7739	$-2.475 \cdot 10^{-4}$	$9.056 \cdot 10^{-4}$

Table 4.10: Coupling coefficients obtained from the APES minima.

Compound	$E_1 \; (\mathrm{meV})$	$E_2 \; (\mathrm{meV})$	$3\Gamma~(\mathrm{meV})$	ω (THz)	T (ps)
NaCl:Rh ²⁺	0.000	0.026	0.026	0.0388	162.074
${ m MgO:Cu^{2+}}$	0.000	76.015	76.015	115.487	0.054
$MgO:Ag^{2+}$	0.040	44.049	44.049	66.922	0.094
CaO:Cu ²⁺	0.014	19.051	19.051	28.944	0.217
$CaO:Ag^{2+}$	0.001	26.053	26.053	39.582	0.159
$SrO:Cu^{2+}$	0.001	11.356	11.356	17.253	0.364
$SrO:Ag^{2+}$	0.002	4.385	4.385	6.6632	0.943
Na_3	0.000	0.548	0.548	0.833	7.541
K_3	0.000	0.280	0.280	0.425	14.781
Cu_3	0.000	5.371	5.371	8.160	0.770
Ag_3	0.000	1.026	1.026	1.559	4.030

Table 4.11: Results for the unit cell energy of the first two excited states, tunneling splitting and angular velocity and period of oscillations in some compounds. Ground state energy is not shown since energies are set relative to the ground state energy.

E states (Reference energy and E_1 in Figure 4.11) and the non-degenerate A_1 state (E_2). This is the expected behavior in systems that exhibit a geometrical phase [5].

As for the oxides, they exhibit the shortest oscillations among the studied compounds. MgO is the stiffest lattice amongst the ones considered [26], while CaO and SrO follow with softer lattices. This is reflected in the fact that their distortion radii (Q_e, Q_c) in Table 4.7) are the shortest. Stiff lattices favor a higher tunneling splitting (3 Γ), and therefore a higher oscillation frequency. This is an indicative that the energy barrier may be lower than in other compounds and thus the potential energy surface is more akin to a mexican hat. Thus the state is almost free to move along the trough of the APES, and the oscillation is faster. In these cases, the main contribution to total energy is from the kinetic energy more than the potential energy [26, 27]. Although the values for the tunneling splitting are higher than the ones obtained in the references [26, 27], they are within the order of magnitude. Qualitatively, stiffer lattices seem to have faster oscillations, possibly due to the ligands being barely affected by impurities, and almost no local distortion is observed. This trend is observed in the oxides selected, showing that the softer the lattices the longer the oscillations. It is worth noting that, generally, Cu^{2+} -doped oxides seem to have higher tunneling splittings than their Ag^{2+} -doped counterparts, except for CaO. This behavior is also supported in references [26, 27], where even CaO exhibits a similar

trend. Further research in this topic is recommended, with energy profiles obtained from scratch instead of existent data.

For triatomic molecules, lower tunneling splittings, and their corresponding longer oscillation periods, are observed with respect to the oxides. The shortest oscillation is found in Cu_3 , which is similar to that of Cu^{2+} -doped SrO, the softest of the oxides. These oscillations span a few picoseconds. Although they are still faster than typical vibrational modes in larger molecules, they are significantly slower than the oscillations observed in the oxides. The fast oscillation frequency may be caused by the small barrier of these compounds in Table 4.10. In these compounds the kinetic energy is probably the main contributor to the tunneling splitting as well, however, having softer bonds than the ionic bonds in the oxides (larger distortion radii), the oscillation is slower. Amongst the trimer molecules selected, K_3 shows the slowest oscillation.

Lastly, for the Rh^{2+} impurities in NaCl, the oscillation periods are significantly longer than those observed in the oxides and triatomic molecules. Local distortions for this complex are larger than those in the other systems, which contributes to the longer oscillation periods. Moreover, since the value of |G| in Table 4.10 is comparable to V and K, it is expected to have a significant energy barrier.

Chapter 5

Conclusions

In this work, we have studied the nuclear dynamics associated to Jahn-Teller systems as a central phenomenon in various materials, highlighting its impact on the electronic structure and vibrational dynamics. In particular, we have studied the vibronic coupling theory necessary to the understanding of the $E \otimes e$ Jahn-Teller problem, which has been the central part of the work, as well as the computational methods employed to analyze the tunneling dynamics in different systems from a theoretical and computational standpoint, providing insights into their behavior and properties. A computational solution was developed to account for the vibronic coupling effects in the studied systems.

The main results of this work include a comprehensive analysis of the tunneling dynamics and the obtention of the frequency of oscillatory JT distortions in various materials, including perovskites, impurities in oxides, and triatomic molecules. The results indicate that the oscillation periods vary significantly among the studied systems, ranging from picoseconds in oxides to hundreds of picoseconds in impurities like Rh²⁺ in NaCl. These findings suggest that the dynamics of Jahn-Teller systems can manifest differently depending on the material's properties, such as lattice stiffness.

Regarding KCuF₃, the prototypical example of a Jahn-Teller system, an energetic profile was obtained by doing a number of simulations with the CRYSTAL software. This profile was used to obtain precise values of the coupling coefficients that characterize the system's APES. Two studies have been carried out on KCuF₃: one focusing on the JT nature of this solid-state system and the other studying the influence of electronic motion over the nuclear tunneling dynamics with respect to a non-JT counterpart. The numerical values obtained from these studies suggest that frequency of the oscillations is of the same order as in a non-JT model, but the physical properties inherent to a JT system, such as the geometrical phase, cannot be captured by such a model.

As for the other systems studied, they exhibit a range of behaviors that highlight the diversity of the dynamics of Jahn-Teller systems across different materials. The oxides studied show a trend where stiffer lattices lead to faster oscillations. Triatomic molecules, on the other hand, display slower oscillations, making them more amenable to experimental observation. The frequency of oscillations for KCuF₃ falls within the intermediate range of a few picoseconds observed for the triatomic molecules, with a period of T=4.343 ps. The Rh²⁺ impurities in NaCl, with their significantly longer oscillation periods, represent the slowest dynamics among the systems studied, making them the most viable for detection with standard experimental techniques.

This work highlights the importance of electronic properties of the system in determining energy barriers, and therefore the tunneling dynamics and the manifestation of the tunneling Jahn-Teller dynamics, on materials. Additionally, elastic properties like lattice stiffness also play a crucial role in shaping the potential energy surfaces.

Appendix A

JT System Python Code

```
1 " " "
 2 Programa que calcula los estados y energías de un sistema Jahn-Teller.
 3 @author: Pablo Miguel Rubio
4 @date: Junio 2025
6 import numpy as np
7 import matplotlib.pyplot as plt
8 from scipy.sparse import diags, kron, bmat, csr_matrix
9 from scipy.sparse.linalg import eigsh
11 # Constantes físicas
12 cons_V = 1 # eV/Å
13 cons_K = 1 # eV/Å^2
14 \text{ cons}_{V2} = 0.0 \# eV/Å^2
15 cons_G = 1 # eV/Å^3
16 cons_H = 1 # eV/Å^4
_{17} masa = 1 # UMA
18 x_max = 1 # Å
19
N_{part} = 100
22 # Lista de estados a graficar
23 estados_elegidos = range(3)
24 n_estados = len(estados_elegidos)
28 # Pasar a UA
29 cons_V *= (0.529177249)/27.2117 # Ha/Bohr
30 cons_K *= (0.529177249 ** 2)/27.2117 # Ha/Bohr^2
31 cons_V2 *= (0.529177249 ** 2)/27.2117 # Ha/Bohr^2
32 cons_G *= (0.529177249 ** 3)/27.2117 # Ha/Bohr^3
33 cons_H *= (0.529177249 ** 4)/27.2117 # Ha/Bohr^4
34 masa *= 1822.88839 # masa en unidades atómicas
35 x_max /= 0.529177249 # Bohr
37 N = (2 * N_part + 1) ** 2 # Número de puntos en la malla
x = \text{np.linspace}(-x_{\text{max}}, x_{\text{max}}, 2 * N_{\text{part}} + 1)
41 # Para graficar en Ångstroms
x_{angstrom} = x * 0.529177249
43 X_ang, Y_ang = np.meshgrid(x_angstrom, x_angstrom)
45 delta=x[1]-x[0]
46 \text{ kin} = 0.5/\text{masa/delta**2}
```

```
48 # Operadores de derivadas segundas
49 bloque_D2x = diags([-2, 1, 1], [0, 1, -1], shape=(2 * N_part + 1, 2 * N_part +
      1))
50 D2x = kron(diags([1], [0], shape=(2 * N_part + 1, 2 * N_part + 1)), bloque_D2x)
51 D2y = diags([-2, 1, 1], [0, (2 * N_part + 1), -(2 * N_part + 1)], shape=(N, N))
T_{cin} = -kin * (D2x + D2y)
54 def construir_bloque(f):
55
      Construye un bloque diagonal a partir de una función f(x, y).
56
57
      bloque = np.zeros((N,))
58
      for j in range(2 * N_part + 1):
59
          for i in range(2 * N_part + 1):
60
              idx = j * (2 * N_part + 1) + i
61
              x = (i - N_part) * delta
              y = (j - N_{part}) * delta
              bloque[idx] = f(x, y)
64
65
      return diags(bloque)
67 # Construcción de los bloques del Hamiltoniano
H_th_th = construir_bloque(lambda x, y: -cons_V * x + (cons_K/2) * (x**2 + y**2)
       + cons_G * x * (x**2 - 3 * y**2) + cons_V2 * (x**2 - y**2) + cons_H * (x**2)
       + y**2)**2)
69 H_th_eps = construir_bloque(lambda x, y: cons_V * y + 2 * cons_V2 * x * y)
70 H_eps_eps = construir_bloque(lambda x, y: cons_V * x + (cons_K/2) * (x**2 + y
      **2) + cons_G * x * (x**2 - 3 * y**2) - cons_V2 * (x**2 - y**2) + cons_H * (
      x**2 + y**2)**2)
71
72 # Hamiltoniano completo
73 Hamiltoniano = bmat([[T_cin + H_th_th, H_th_eps], [H_th_eps, T_cin + H_eps_eps
      ]], format='csr')
74
75 autovalores, autovectores = eigsh(Hamiltoniano, k=n_estados, which='SA')
76 autovalores = (autovalores - autovalores[0]) * 27.2117 * 1000 # Convertir a meV
78
79 print("Energies (meV):")
80 for i, energia in enumerate (autovalores):
      print(f"State {i}: {energia:.8f} meV")
83 TresGamma = (autovalores[2] - autovalores[0])/1e3 # Convertir a eV
84 frecuencia = TresGamma / (4.135667696e-15*1e12/(2*np.pi))
85 periodo = 2 * np.pi / frecuencia
86 print(f"3Gamma: {TresGamma:.8f} eV")
87 print(f"Frecuencia de oscilación: {frecuencia:.8f} rad/ps")
88 print(f"Período de oscilación: {periodo:.8f} ps")
91 # Graficar los estados
92 n_cols = n_estados
n_rows = 2
94 fig, axes = plt.subplots(n_rows, n_cols, figsize=(5 * n_cols, 10))
95 axes = axes.flatten()
97 for idx, estado in enumerate(estados_elegidos):
      estado_vector = autovectores[:, estado]
98
      # Chi_theta
      estado_matriz_superior = np.reshape(estado_vector[:N], (2 * N_part + 1, 2 *
      N_{part} + 1)
      vmax = max(abs(estado_matriz_superior.min()), abs(estado_matriz_superior.max
      ()))
```

```
ax_superior = axes[idx]
103
              ax\_superior.set\_title(f"State {estado} - \theta \nEnergy: {autovalores[estado]:.8}
104
             f} meV")
              c1 = ax_superior.imshow(estado_matriz_superior, cmap="seismic", extent=[
105
             x_angstrom[0], x_angstrom[-1], x_angstrom[0], x_angstrom[-1]], origin='lower
             ', interpolation='none', vmin=-vmax, vmax=vmax)
              fig.colorbar(c1, ax=ax_superior)
107
              # Chi_epsilon
108
              \tt estado\_matriz\_inferior = np.reshape(estado\_vector[N:], (2 * N\_part + 1, 2 
109
             N_part + 1))
              vmax = max(abs(estado_matriz_inferior.min()), abs(estado_matriz_inferior.max
110
              ax_inferior = axes[idx + n_cols]
111
              ax_inferior.set_title(f"State {estado} - \varepsilon \nEnergy: {autovalores[estado]:.8}
112
             f} meV")
              c2 = ax_inferior.imshow(estado_matriz_inferior, cmap="seismic", extent=[
             x_angstrom[0], x_angstrom[-1], x_angstrom[0], x_angstrom[-1]], origin='lower
                , interpolation='none', vmin=-vmax, vmax=vmax)
              fig.colorbar(c2, ax=ax_inferior)
114
115
plt.tight_layout(pad=4.0)
plt.show()
118
119
120 # plotear H_vib
121 H_th_th_diag = H_th_th.diagonal()
122 H_th_eps_diag = H_th_eps.diagonal()
H_eps_eps_diag = H_eps_eps.diagonal()
125 # Calcular la hoja inferior
126 H_vib_matrix = 0.5 * (H_th_th_diag + H_eps_eps_diag - np.sqrt((H_th_th_diag -
             H_eps_eps_diag)**2 + 4 * H_th_eps_diag**2))
127
128 # Busca los indices del valor minimo
129 min_index = np.argmin(H_vib_matrix)
131 x_min = (min_index % (2 * N_part + 1) - N_part)
x_min_angstrom = x_min * delta * 0.529177249 # Convertir a Ångstrom
133 y_min = (min_index // (2 * N_part + 1) - N_part)
134 y_min_angstrom = y_min * delta * 0.529177249 # Convertir a Angstrom
135 Radio_min = np.linalg.norm([x_min_angstrom, y_min_angstrom])
136 print(f"x_min: {x_min_angstrom:.8f} Å, y_min: {y_min_angstrom:.8f} Å, Radio mí
             nimo: {Radio_min:.8f} A")
137
138
139 # Reformatear para graficar
140 H_vib_matrix = H_vib_matrix.reshape((2 * N_part + 1, 2 * N_part + 1))
141
142 # Graficar H_vib
143 fig, ax = plt.subplots()
144 contour = ax.contour(X_ang, Y_ang, H_vib_matrix, 1000, cmap="viridis")
ax.set_aspect('equal', adjustable='box')
# ax.set_title("Hamiltoniano Vibracional $H_{vib}$")
147 fig.colorbar(contour, ax=ax)
148 plt.show()
```

Appendix B

Non-JT System Python Code

```
1 000
2 Programa que calcula los estados y energías de un sistema no Jahn-Teller.
3 @author: Pablo Miguel Rubio
4 @date: Junio 2025
6 import numpy as np
7 import matplotlib.pyplot as plt
8 from scipy.sparse import diags, kron
9 from scipy.sparse.linalg import eigsh
10
11 # Constantes físicas
cons_K = 5.15404493 \# eV/Å^2
13 \text{ cons}_{G} = -2.80444636
                        # eV/Å^3
14 cons_H = 195.6886573
_{15} masa = 159.6395 # UMA
16 x_max = 0.3 \# Å
N_part = 100
20 # Lista de estados a graficar
21 estados_elegidos = range(3)
22 n_estados = len(estados_elegidos)
26 # Pasar a UA
27 cons_K *= (0.529177249 ** 2)/27.2117 # Ha/Bohr^2
28 cons_G *= (0.529177249 ** 3)/27.2117 # Ha/Bohr^3
29 cons_H *= (0.529177249 ** 4)/27.2117 # Ha/Bohr^4
masa *= 1822.88839 # masa en unidades atómicas
31 x_max /= 0.529177249 # Bohr
32
33 N = (2 * N_part + 1) ** 2 # Número de puntos en la malla
34
x = np.linspace(-x_max, x_max, 2 * N_part + 1)
36 # Para graficar en Ångstroms
x_{angstrom} = x * 0.529177249
38 X_ang, Y_ang = np.meshgrid(x_angstrom, x_angstrom)
41 delta=x[1]-x[0]
42 \text{ kin} = 0.5/\text{masa/delta**}2
44 # Operadores de derivadas segundas
45 bloque_D2x = diags([-2, 1, 1], [0, 1, -1], shape=(2 * N_part + 1, 2 * N_part +
46 D2x = kron(diags([1], [0], shape=(2 * N_part + 1, 2 * N_part + 1)), bloque_D2x)
```

```
47 D2y = diags([-2, 1, 1], [0, (2 * N_part + 1), -(2 * N_part + 1)], shape=(N, N))
48 T_cin = -kin * (D2x + D2y)
49
50 def construir_bloque(f):
       Construye un bloque diagonal a partir de una función f(x, y).
52
53
       bloque = np.zeros((N,))
54
       for j in range(2 * N_part + 1):
55
           for i in range(2 * N_part + 1):
56
               idx = j * (2 * N_part + 1) + i
57
               x = (i - N_part) * delta
58
               y = (j - N_part) * delta
59
               bloque[idx] = f(x, y)
60
       return diags(bloque)
61
65 H_vib = construir_bloque(lambda x, y: - cons_K * (x**2 + y**2) + cons_H * ((x**2
       + y**2) ** 2) + cons_G * x * (x**2 - 3 * y**2))
67 # Hamiltoniano completo
68 Hamiltoniano = T_cin + H_vib
70 autovalores, autovectores = eigsh(Hamiltoniano, k=n_estados, which='SA')
71 autovalores = (autovalores - autovalores[0]) * 27.2117 * 1000 # Convertir a meV
73 print("Energies (meV):")
74 for i, energia in enumerate (autovalores):
       print(f"State {i}: {energia:.8f} meV")
76
77 TresGamma = (autovalores[2] - autovalores[0])/1e3 # Convertir a eV
78 frecuencia = TresGamma / (4.135667696e-15*1e12/(2*np.pi))
79 periodo = 2 * np.pi / frecuencia
80 print(f"3Gamma: {TresGamma:.8f} eV")
81 print(f"Frecuencia de oscilación: {frecuencia:.8f} rad/ps")
82 print(f"Período de oscilación: {periodo:.8f} ps")
84 # Graficar los estados
n_{cols} = (n_{estados})
n_rows = 1
87 fig, axes = plt.subplots(n_rows, n_cols, figsize=(5 * n_cols, 4))
88 axes = axes.flatten()
90 for idx, estado in enumerate(estados_elegidos):
       estado_vector = autovectores[:, estado]
91
92
       estado_matriz = -np.reshape(estado_vector, (2 * N_part + 1, 2 * N_part + 1))
      .transpose()
       vmax = max(abs(estado_matriz.min()), abs(estado_matriz.max()))
94
       axis = axes[idx]
95
       axis.set_title(f"State {estado} \nEnergy: {autovalores[estado]:.8f} meV")
96
      c1 = axis.imshow(estado_matriz.T, cmap="seismic", extent=[x_angstrom[0],
97
      x_angstrom[-1], x_angstrom[0], x_angstrom[-1]], origin='lower',
      interpolation='none', vmin=-vmax, vmax=vmax)
98
       fig.colorbar(c1, ax=axis, orientation='vertical')
plt.tight_layout(pad=4.0)
101 plt.show()
```

Bibliography

- [1] Cohen-Tannoudji, C., Diu, B., and Laloë, F. Quantum Mechanics. Wiley, 1973.
- [2] Kogan, E. Quantum Mechanics II. Course by E. Kogan. 2019.
- [3] Gordon, J. P., Zeiger, H. J., and Townes, C. H. "The Ammonia Maser—New Type of Microwave Amplifier, Frequency Standard, and Spectrometer". In: *Physical Review* 99 (1955), pp. 1264–1274. DOI: 10.1103/PhysRev.99.1264.
- [4] Bersuker, I. B. Jahn-Teller Effect. Cambridge University Press, 2006.
- [5] Ham, F. S. "Berry's Geometrical Phase and the Sequence of States in the Jahn-Teller Effect". In: *Physical Review Letters* 58 (1986), pp. 725–728. DOI: 10.1103/PhysRevLett. 58.725.
- [6] Gehring, G. A. and A., Gehring K. "Co-operative Jahn-Teller effects". In: Reports Progress in Physics 38.1 (1975). DOI: 10.1088/0034-4885/38/1/001.
- [7] Goodenough, J. B. "JAHN-TELLER PHENOMENA IN SOLIDS". In: Annual Review of Materials Research 28 (1998), pp. 1–27. DOI: 10.1146/annurev.matsci.28.1.1.
- [8] Wang, S., Guo, X., Huang, K., et al. "Cooperative Jahn-Teller effect and engineered long-range strain in manganese oxide/graphene superlattice for aqueous zinc-ion batteries". In: *Nature Communications* 16.5191 (2025). DOI: 10.1038/s41467-025-60558-y.
- [9] Fernández-Ruiz, T. et al. "Many-body model for the cooperative Jahn-Teller effect in crystals and its associated orbital ordering". In: *Physical Review B* 109.205150 (2024). DOI: 10.1103/PhysRevB.109.205150.
- [10] Fernández-Ruiz, T. et al. "Strain-Phonon Cooperation as a Necessary Ingredient to Understand the Jahn-Teller Effect in Solids". In: *The Journal of Physical Chemistry Letters* 15.25 (2024), pp. 6476–6481. DOI: 10.1021/acs.jpclett.4c01256.
- [11] Griffith, J. S. The Irreducible Tensor Method for Molecular Symmetry Groups. Dover Publications, 2006.
- [12] Berry, M. V. Quantal Phase Factors Accompanying Adiabatic Changes. Vol. 392. 1802. 1984, pp. 45–57. DOI: 10.1098/rspa.1984.0023.
- [13] García-Fernández, P. et al. "Origin of warping in the E⊗e Jahn-Teller problem: Quadratic vibronic coupling versus anharmonicity and application to NaCl: Rh²⁺ and triangular molecules". In: *Physical Review B* 71.18 (2005). DOI: 10.1103/physrevb.71.184117.
- [14] Jensen, F. Introduction to Computational Chemistry. 2nd ed. New York: John Wiley & Sons, 1999.
- [15] Szabo, A. and Ostlund, N. S. Modern Quantum Chemistry: Introduction to Advanced Electronic Structure Theory. Dover Publications, 1996.
- [16] García-Fernández, P. Estructuras de Moléculas y Sólidos. Apuntes de clase, Universidad de Cantabria. 2025.
- [17] Hohenberg, P. and Kohn, W. "Inhomogeneous electron gas". In: *Physical Review* 136 (1964), B864–B871. DOI: 10.1103/PhysRev.136.B864.

56 BIBLIOGRAPHY

[18] Kohn, W. and Sham, L. J. "Self-Consistent Equations Including Exchange and Correlation Effects". In: *Physical Review* 140 (1965), A1133–A1138. DOI: 10.1103/PhysRev.140. A1133.

- [19] Koch, W. and Holthausen, M. C. A Chemist's Guide to Density Functional Theory. Wiley-VCH, 2001.
- [20] Thomas, L. H. "The Calculation of Atomic Fields". In: Mathematical Proceedings of the Cambridge Philosophical Society 23 (1927), pp. 542–548. DOI: 10.1017/S0305004100011683.
- [21] Fermi, E. "Un Metodo Statistico per la Determinazione di alcune Prioprietà dell'Atomo". In: *Endiconti: Accademia Nazionale dei Lincei* 6 (1927), pp. 602–607.
- [22] Erba, A. et al. "CRYSTAL23: A Program for Computational Solid State Physics and Chemistry". In: *Journal of Chemical Theory and Computation* (2022).
- [23] Bilc, D. I., Orlando, R., Shaltaf, R., et al. "Hybrid exchange-correlation functional for accurate prediction of the electronic and structural properties of ferroelectric oxides". In: *Physical Review B* 77.16 (2008), p. 165107. DOI: 10.1103/PhysRevB.77.165107.
- [24] Monkhorst, H. J. and Pack, J. D. "Special points for Brillouin-zone integrations". In: *Physical Review B* 13 (1976), pp. 5188–5192. DOI: 10.1103/PhysRevB.13.5188.
- [25] García-Fernández, P. et al. "Coherent tunneling in Cu²⁺- and Ag²⁺-doped MgO and CaO: Cu²⁺ explored through ab initio calculations". In: *Physical Review B* 72.15 (2005). DOI: 10.1103/physrevb.72.155107.
- [26] García-Fernández, P. et al. "Tunneling Splitting of Jahn-Teller Ions in Oxides". In: *Physical Review Letters* 104 (3 2010), p. 035901. DOI: 10.1103/PhysRevLett.104.035901.
- [27] García-Fernández, P. et al. "Dynamic and Static Jahn-Teller Effect in Impurities: Determination of the Tunneling Splitting". In: 2011, pp. 105–142. ISBN: 978-94-007-2383-2. DOI: 10.1007/978-94-007-2384-9_6.